Theory of angle-resolved photoemission spectroscopy in graphene-based moiré superlattices

Jihang Zhu, Jingtian Shi , and Allan H. MacDonald Department of Physics, University of Texas at Austin, Austin, Texas 78712, USA

(Received 11 August 2020; revised 1 May 2021; accepted 9 June 2021; published 22 June 2021)

Graphene-based moiré superlattices are now established as an interesting platform for strongly correlated many-electron physics, and they have so far been characterized mainly by transport and scanning tunneling microscopy (STM) measurements. Motivated by recent experimental progress, we present a theoretical model study whose aim is to assess the potential of angle-resolved photoemission spectroscopy (ARPES) to resolve some of the many open issues in these systems. The theory is developed specifically for graphene on hexagonal boron nitride (G/hBN) and twisted bilayer graphene (TBG) moiré superlattices, but it is readily generalized to any system with active degrees of freedom in graphene sheets.

DOI: 10.1103/PhysRevB.103.235146

I. INTRODUCTION

A large body of theoretical and experimental work [1,2] over the past decade has achieved a thorough understanding of most single-layer and few-layer graphene film properties. Progress in this field has been aided by success in reducing disorder effects to very low levels and by the identification of hexagonal boron nitride (hBN) [3-5], with its large band gaps and atomically smooth surfaces, as the substrate of choice. The recent discovery of superconducting, correlated insulating, and orbital magnetic states in magic-angle [6] twisted bilayer graphene (MATBG) [7–12] has now added strongly correlated-electron behavior to the physics that can be explored in graphene multi-layers. MATBG's strong-correlation physics is a consequence of unusual flat-band behavior near a discrete set of magic twist angles [6]. The flat bands emerge from interference between intralayer and interlayer hopping processes that are individually strong. The residual dispersion in these bands is important for understanding physical properties but, because it results from a delicate cancellation, is difficult to predict reliably on the basis of theoretical considerations alone. The difficulty of quantitative theoretical modeling is heightened by the large number of carbon atoms $(\sim 10^4)$ per superlattice unit cell, by the important role of interactions in reshaping the moiré superlattice bands [13–15], by the critical importance of nonlocal exchange interactions [14], and by a tendency toward spin and/or valley flavor symmetry breaking [14–18] that is still incompletely understood. Because ARPES directly probes the momentum-dependence of the one-particle electronic Green's function, it is uniquely positioned to guide progress toward a quantitative understanding of MATBG properties.

ARPES has become an indispensable tool for studies of strongly interacting [19–21] and topological materials [22], and has been applied successfully to single-layer and multilayer epitaxial graphene samples formed on the surface of silicon carbide [23–34]. The typical photon beam spot size of conventional ARPES experiments is \sim 25–100 μ m [35],

larger than or roughly equal to the \sim 1–100 μ m size of typical MATBG samples prepared by mechanical exfoliation of two-dimensional (2D) crystals. Applying the power of ARPES to MATBG physics requires either access to the nano length scale in ARPES, or larger moiré samples. Recent progress in nano-ARPES [36–42] may provide the necessary opening and has been implemented to mechanically exfoliated van der Waals heterostructures [43–49]. Preliminary applications of nano-ARPES to G/hBN [48] and TBG moiré superlattices [33,49–51] have been reported recently.

The ARPES spectra of graphene moiré systems have been studied previously using both tight-binding model [52,53] and continuum model approaches [54,55]. In this paper we use an accurate continuum model to compute theoretical ARPES spectra of both G/hBN and MATBG with the goal of informing the interpretation of future ARPES experiments, either nano-ARPES studies of MATBG samples similar to those that are currently available or conventional ARPES studies of large area MATBG samples which could become available in the future. We find that key parameters of low-energy effective models, like the size of mass term that expresses broken inversion symmetry in G/hBN and the G/G interlayer intrasublattice and intersublattice tunneling parameters, can be inferred from ARPES momentum distributions. Although a complete treatment of the role of interactions lies out of the scope of this paper, we do comment on the ability of ARPES to measure flat-band shape renormalization by electron-electron interactions, and the broken spin and/or valley flavor symmetries thought to occur at fractional flat band filling.

This paper is organized as follows. In Sec. II we discuss the general theory of ARPES in graphene-based moiré superlattices described by $\mathbf{k} \cdot \mathbf{p}$ continuum models. In Secs. III and IV we focus on two prototypical moiré superlattice systems, G/hBN in which ARPES can be used to determine the important inversion symmetry breaking mass parameter, and TBG in which ARPES can characterize strain relaxation within the moiré pattern and identify when the

magic angle is reached. In the latter case, important parameters can be identified by performing measurements of momentum space distributions at energies well away from the flat bands that do not require extremely precise energy resolution. In Sec. V, we discuss ARPES momentum distributions at van Hove singularity (VHS) energies in TBG, which can be revealed in both large and small twist angle regimes. Finally in Sec. VI we conclude with a general discussion of some of the issues that could be clarified if accurate ARPES measurements become a possibility.

II. ARPES IN GRAPHENE-BASED MOIRÉ SUPERLATTICES

The ARPES intensity $I(\mathbf{p}, E)$ is proportional to the transition probability from a Bloch initial state with crystal momentum \mathbf{k} and energy E to a photoelectron final state with momentum \mathbf{p} and kinetic energy $E_{\rm kin}$. Energy conservation guarantees $E_{\rm kin} = \hbar\omega + E - \phi$, where $\hbar\omega$ is the photon energy and ϕ is the work function. The initial state energy E is relative to the Fermi energy. In noninteracting electron models the ARPES spectrum of a 2D solid is nonzero only if one of the occupied band states at momentum \mathbf{k} , where \mathbf{k} is the in-plane projection \mathbf{p}_{\parallel} reduced to the 2D Brillouin zone (BZ), has energy E. The intensity of the peak produced by an occupied band state at a given extended zone momentum replica depends on the Bloch state wave function. This dependence is particularly simple when all the states of interest are linear combinations of carbon π -orbitals on different lattice sites, as we now explain.

The moiré superlattice period of G/hBN multilayers depends on both the lattice constant mismatch and twist angle between the graphene and hBN layers, whereas the moiré superlattice period of TBG depends only on twist angle. In both G/hBN and TBG cases we will assume near perfect alignment so that the moiré modulation has a long wavelength. Since we are interested in electronic states at energies near the Dirac point we can use $\mathbf{k} \cdot \mathbf{p}$ continuum models [6] in which π -orbital envelope function spinors satisfy effective Schrodinger equations. The number of components of the envelope function spinors is two (for the two honeycomb sublattices) times the number of active graphene layers in the moiré heterojunction. At low energies the correction to the Dirac Hamiltonians of isolated graphene layers can be approximated by a sublattice and position-dependent terms that have the periodicity of the moiré pattern. For example, these have been detailed for the G/hBN and TBG cases discussed below in Refs. [6,56–58]. In the TBG case, the moiré superlattice is defined mainly by the spatial pattern of interlayer tunneling, whereas in the G/hBN case the moiré superlattice is defined by the spatial pattern of sublattice-dependent energies and inter-sublattice tunneling.

Specializing to the case in which a single graphene layer is active, the initial electronic states prior to photoemission are moiré band eigenstates $|\xi, n, \mathbf{k}\rangle$, two-component sublattice spinors that have a Bloch state plane-wave expansion:

$$|\xi, n, \mathbf{k}\rangle = \sum_{\alpha, \mathbf{g}} \psi_{n\alpha\mathbf{g}}^{\xi}(\mathbf{k}) |\mathbf{k} + \mathbf{g}, \alpha\rangle.$$
 (1)

Here $\xi = \pm$ is a valley index, n is a band index, \mathbf{g} is a moiré reciprocal lattice vector, $|\mathbf{k}, \alpha\rangle$ is a graphene π -orbital state with definite sublattice $\alpha = A$, B and momentum \mathbf{k} . In the calculations below we cut-off the momentum expansion at $\mathbf{g} \in \{\mathbf{0}, \mathbf{g}_1, \dots, \mathbf{g}_6\}$ for G/hBN, where $\mathbf{g}_1, \dots, \mathbf{g}_6$ are the six first-shell moiré reciprocal lattice vectors. For TBG case, we include three shells of moiré reciprocal lattice vectors, i.e., $|\mathbf{g}_{\max}| = 3g$ where g is the length of the primitive reciprocal lattice vector.

When multilayer graphene is probed using high-energy photon beams, in the soft x-ray regime, for example, the photoemission final state is well approximated as free-electron [59] and photoelectron scattering and diffraction effects can be ignored. This approximation is justified because (i) the crystal potential is relatively small compared to the photoelectron's kinetic energy [60], (ii) the scattering cross section is small for light atoms [61], and (iii) π -orbitals in graphene form delocalized itinerant band states [62]. Indeed, the freeelectron final state approximation has worked very well in previous studies [52,54,63,64]. Note that the photon energy should be high but not too high, because high-photon-energy decreases the energy resolution and momentum resolution. The neglected final state effects [32,65–67] can be important at low photon energies (\$\leq 50 \text{ eV}\right), but are out of the scope of this paper.

By generalizing the established theory [68] of monolayer graphene sheet ARPES intensity summarized in Appendix A, where matrix element effects that are dependent on experimental geometry are ignored and a free-electron final state is assumed, we obtain the following expression for the dependence of the ARPES signal on the initial Bloch state energy E and photoelectron momentum \mathbf{p} :

$$I(\mathbf{p}, E) \propto \sum_{\xi, n, \mathbf{k}} |\langle \mathbf{p} | \xi, n, \mathbf{k} \rangle|^2 \delta \left(E - \varepsilon_{n\mathbf{k}}^{\xi} \right)$$

$$\propto |\phi(\mathbf{p})|^2 \sum_{\xi, n, \mathbf{k}} \delta \left(E - \varepsilon_{n\mathbf{k}}^{\xi} \right)$$

$$\times \left| \sum_{\alpha, \mathbf{g}} \psi_{n\alpha\mathbf{g}}^{\xi}(\mathbf{k}) e^{-i\mathbf{G} \cdot \mathbf{\tau}_{\alpha}} \delta_{\mathbf{p}_{\parallel}, \mathbf{k} + \mathbf{g} + \mathbf{G}} \right|^2, \qquad (2)$$

where $\phi(\mathbf{p}) = \int d^3\mathbf{r}e^{-i\mathbf{p}\cdot\mathbf{r}}\phi(\mathbf{r})$ is the Fourier transform of the atomic π -orbital and \mathbf{G} is a reciprocal lattice vector of an isolated graphene layer. Equation (2) ignores a factor related to photon polarization. A given photoelectron momentum \mathbf{p} picks a specific \mathbf{G} , valley wavevector \mathbf{K}_ξ , and moiré reciprocal lattice vector \mathbf{g} to map $\mathbf{k} = \mathbf{p}_{\parallel} - \mathbf{g} - \mathbf{G}$ into the moiré Brillouin zone (MBZ). Below we assume that \mathbf{p}_{\parallel} is near the $\mathbf{K}_+ = (4\pi/3a, 0)$, where a is graphene's lattice constant, Eq. (2) simplifies to

$$I(\mathbf{p}, E) \propto |\phi(\mathbf{p})|^2 \sum_{n,\mathbf{k}} \left| \sum_{\alpha,\mathbf{g}} \psi_{n\alpha\mathbf{g}}^+(\mathbf{k}) \delta_{\mathbf{p}_{\parallel},\mathbf{k}+\mathbf{g}} \right|^2 \delta(E - \varepsilon_{n\mathbf{k}}^+).$$
 (3)

Photon polarization effects [31,69] add a momentumdependent weighting factor and can alter momentum distribution function anisotropy. When they are taken into account using the dipole approximation, as summarized in Appendix A, we obtain

$$I(\mathbf{p}, E) \propto \sum_{\xi, n, \mathbf{k}} |\langle \mathbf{p} | \mathbf{A} \cdot \hat{\mathbf{v}} | \xi, n, \mathbf{k} \rangle|^2 \delta(E - \varepsilon_{n\mathbf{k}}^{\xi})$$

$$= \mathbf{A} \cdot \sum_{\xi, n, \mathbf{k}} |\langle \mathbf{p} | \nabla_{\mathbf{k}} H | \xi, n, \mathbf{k} \rangle|^2 \delta(E - \varepsilon_{n\mathbf{k}}^{\xi}), \quad (4)$$

where the free-electron final state is projected to the Bloch basis

$$|\mathbf{p}\rangle = \sum_{\mathbf{k},\mathbf{g},\alpha} \delta_{\mathbf{p}_{\parallel},\mathbf{k}+\mathbf{g}+\mathbf{G}} e^{i\mathbf{G}\cdot\boldsymbol{\tau}_{\alpha}} \phi^{*}(\mathbf{p}) |\mathbf{k}+\mathbf{g},\alpha\rangle.$$
 (5)

In multilayer systems, the out-of-plane momentum component p_z of the photoelectron controls interlayer interferences, which is absent in the single active layer G/hBN case, but included in the TBG case in Sec. IV.

III. GRAPHENE ON HBN

The moiré band structure of graphene on aligned hBN is illustrated in Fig. 1(a). These bands were calculated from a continuum model [57] that accounts for lattice relaxation. In this model low energy states in graphene are most strongly modified by the substrate hBN layer when the two layers are aligned ($\theta = 0^{\circ}$). In this case the inversion symmetry breaking in the presence of hBN opens a gap with size \sim 7 meV [57] at charge neutrality and a gap between the highest-energy valence band and remote valence bands. Both gaps are apparent in transport measurements [70–72]. Figures 1(b)–1(d) show the corresponding ARPES momentum distribution functions near BZ corner \mathbf{K}_{+} , using Eq. (3) in which a factor related to photon polarization is dropped, calculated at an energy near the middle of the highest valence band and at an energy below the energy gap separating this band from lower energy states. For the aligned ($\theta = 0^{\circ}$) case, the hBN substrate has little effect [Fig. 1(b)] on the ARPES spectrum except at energies that are close to the induced gaps on the hole-side [Fig. 1(c)]. In Fig. 1(b) in particular, the constant energy surface is still well inside the MBZ and the ARPES momentum distribution is similar to the circular constant-energy surface of monolayer graphene [26,31,32] shown in Appendix A. At a lower energy illustrated in Fig. 1(c), Bragg scattering by moiré reciprocal lattice vectors thoroughly mixes isolated layer momentum eigenstates and this is reflected in the momentum distribution functions. The avoided crossings that are apparent in Fig. 1(c) are sometimes referred to as secondary Dirac cones [72–78]. When the two layers are not accurately aligned, as in the $\theta = 2^{\circ}$ case illustrated in Fig. 1(d), the unperturbed energy at the MBZ boundary is large, increasing the range of energy over which the ARPES momentum distribution is not strongly altered by hBN. This result agrees with previous ARPES observations [48].

The momentum distribution functions in Fig. 1 are anisotropic as a function of momentum direction. These dark corridor [32] anisotropies are well known from previous ARPES studies of epitaxial graphene systems [27,31,32,55,63,64,68,79] and result from interference between photoemissions from two honeycomb sublattices. The ARPES intensity anisotropy also has a photon-polarization dependence [31,32,80,81] that is ignored when Eq. (3) is

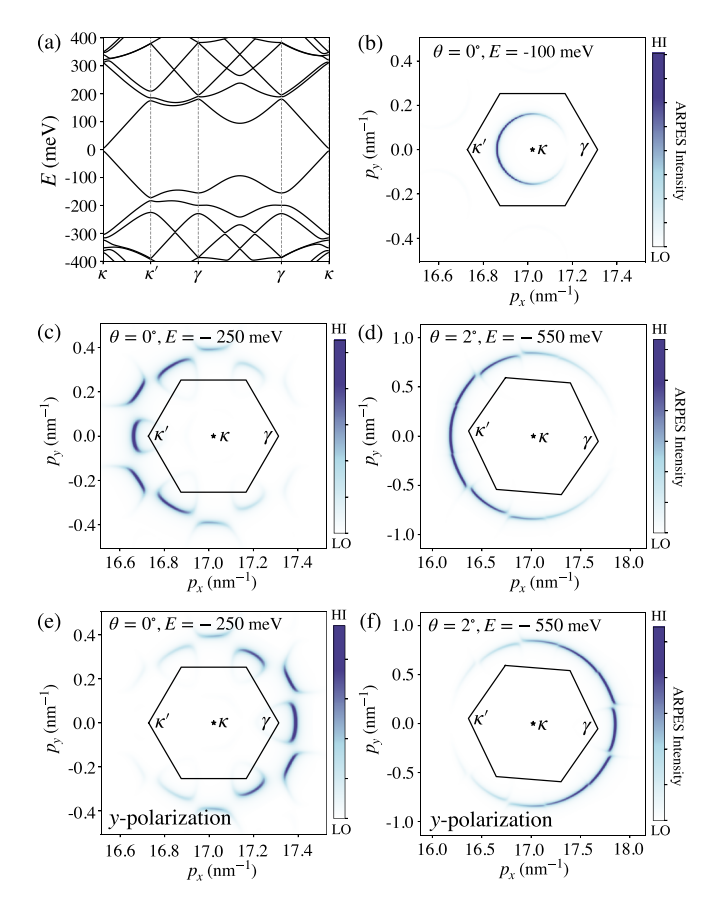


FIG. 1. (a) Moiré band structure of G/hBN with twist angle $\theta=0^\circ$, calculated using the *ab initio* relaxed first harmonic parameters from Ref. [57]. (b)–(d) Constant-energy ARPES momentum distributions near BZ corner \mathbf{K}_+ calculated using Eq. (3) in which a factor related to photon polarization is dropped. (b) $\theta=0^\circ$ at energy E=-100 meV, where hBN substrate has little effect on the energy bands; (c) $\theta=0^\circ$ at energy E=-250 meV, where the hBN substrate has a large effect on the energy bands of graphene; (d) $\theta=2^\circ$ at E=-550 meV. hBN's effect is negligible when the graphene and hBN layers are away from alignment. (e), (f) Constant-energy ARPES momentum distributions calculated for *y*-polarized light using Eq. (4). The *x*-polarized light yields ARPES contours identical to those calculated in (c), (d) using Eq. (3). Photons with *y*-polarization rotate the anisotropy by π compared to photons with *x*-polarization. In (b)–(f), the hexagon is the MBZ.

used for the momentum distribution function, highlighted in Figs. 1(e) and 1(f) which illustrate momentum distributions calculated for the case of *y*-polarized light using Eq. (4). For momenta near \mathbf{K}_+ , the ARPES momentum distribution contour with *x*-polarized light calculated using Eq. (4) is identical to the result obtained using Eq. (3) and shown in Figs. 1(b)–1(d). This is a consequence of the Dirac Hamiltonian property: $\nabla_{\mathbf{k}}H_0 = \hbar v_F(\sigma_x, \sigma_y)$. The same observation applies for the TBG model discussed in Sec. IV, in which interlayer tunneling is momentum independent. The constant-energy ARPES anisotropies of G/hBN using *x*- and *y*-polarized light are analogous to the monolayer graphene case shown in Appendix A, where in both cases photons with *y*-polarization rotate the anisotropy by π compared to photons with *x*-polarization. The photon-polarization dependent ARPES measurements have

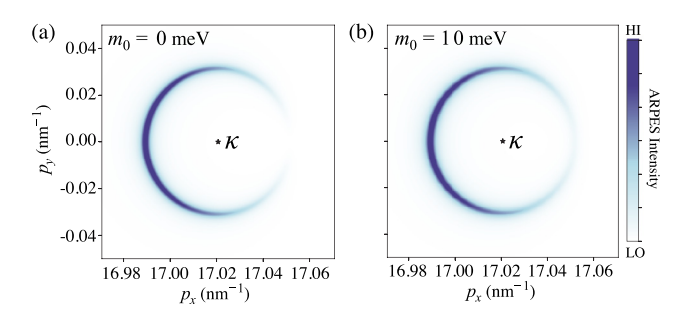


FIG. 2. Constant-energy ARPES maps of 0° -twist G/hBN (a) at $E=-20\,\mathrm{meV}$ for $m_0=0\,\mathrm{meV}$; (b) at $E=-23\,\mathrm{meV}$ for $m_0=10\,\mathrm{meV}$, which produces a band gap $\Delta_{\mathrm{gap}}\sim23\,\mathrm{meV}$ at charge neutrality. The mass parameter m_0 weakens the anisotropy.

been implemented to determine the signs of intralayer and interlayer tunneling parameters in monolayer graphene and Bernal-stacked bilayer graphene [31], as described in Appendix B.

This anisotropy of graphene sheet ARPES can be used to measure one of the key parameters of G/hBN systems, the mass parameter m_0 , as illustrated in Fig. 2. The mass parameter characterizes the strength of sublattice symmetry breaking [82] in graphene and plays a key role in the appearance of the quantized anomalous Hall effect [11,12,83–93]. It has contributions both from single-particle physics and from interacting self-energies, and in the latter case can be spin/valley-flavor dependent [14,15,56–58]. It influences the photoemission by concentrating the quasiparticle states more on one sublattice, thereby weakening sublattice interference and the resulting anisotropy of the APRES signal. When a mass term m_0 is added to the isolated layer Dirac Hamiltonian, the eigenvector becomes

$$\Psi^{\xi}(\mathbf{q}) \propto \begin{pmatrix} e^{-i\xi\theta_{\mathbf{q}}/2} \\ \left(-\frac{m_0}{v_{\rm F}q} + s\sqrt{1 + \frac{m_0^2}{v_{\rm F}^2q^2}} \right) e^{i\xi\theta_{\mathbf{q}}/2} \end{pmatrix}, \tag{6}$$

where \mathbf{q} is momentum measured from the Dirac point, and s=+1(-1) denotes conduction (valence) band. Near \mathbf{K}_+ , the ARPES signal is the square of the sum of the sublattice components of the quasiparticle wave functions. As shown in Fig. 2, the anisotropy is noticeably weaker for $m_0=10\,\mathrm{meV}$ [Fig. 2(b)] than for $m_0=3.62\,\mathrm{meV}$ [57] [Fig. 2(a)]. By comparing the contrast ratio between the weakest and strongest photoemission intensity on the Fermi contour, it should be possible to measure this key parameter.

ARPES momentum distribution functions are influenced both by all details of the single-particle Hamiltonian and by electron-electron interaction effects. Comparing ARPES spectra with theoretical model calculations like those illustrated in Figs. 1(b)–1(f) sheds light on both single-particle and interaction corrections, although they might be difficult to separate. In the case of G/hBN heterojunctions, the questions that ARPES can answer are mostly quantitative in character. We therefore turn now to the case in which ARPES has the greatest potential to answer key qualitative questions, namely the case of TBG heterojunctions, especially close to the magic twist angles.

IV. GRAPHENE ON GRAPHENE

Bilayer graphene moiré superlattices are formed by a relative twist between different graphene sheets. For our TBG calculations, we assume the second layer is twisted clockwise by θ with respect to the first layer. The ARPES momentum distribution function calculations in this section are based on a low-energy continuum moiré Hamiltonian of small-twistangle TBG [6]. ARPES measurements have the potential to validate and refine these models, and to identify important interaction effects. By diagonalizing the continuum model Hamiltonian the miniband Bloch wave functions can be expanded in the form

$$|\xi, n, \mathbf{k}\rangle = \sum_{l,\alpha,\mathbf{g}} \psi_{nl\alpha\mathbf{g}}^{\xi}(\mathbf{k})|\mathbf{k} + \mathbf{g}, l\alpha\rangle$$

$$= \frac{1}{\sqrt{N}} \sum_{l,\alpha,\mathbf{g},\mathbf{R}_{l}} \psi_{nl\alpha\mathbf{g}}^{\xi}(\mathbf{k}) e^{i(\mathbf{k}+\mathbf{g})\cdot(\mathbf{R}_{l}+\tau_{l\alpha})} |\mathbf{R}_{l}, \alpha\rangle, \quad (7)$$

where l=1,2 label layers and $\alpha=A,B$ label sublattices. The coordinates of carbon atoms in two layers are related by $\mathbf{R}_2=\mathcal{R}_{-\theta}(\mathbf{R}_1-\boldsymbol{\tau})+\mathbf{d},~\boldsymbol{\tau}_{2\alpha}=\mathcal{R}_{-\theta}\boldsymbol{\tau}_{1\alpha},$ and \mathcal{R} is the rotation operator. As in the single active layer case, we employ a free electron final state approximation and ignore photon polarization effects to obtain the following expression for the photoemission transition amplitudes:

$$\langle \mathbf{p}|\xi, n, \mathbf{k}\rangle \propto \phi(\mathbf{p}) \sum_{\alpha, \mathbf{g}} \left[\psi_{n1\alpha\mathbf{g}}^{\xi}(\mathbf{k}) \delta_{\mathbf{p}_{\parallel}, \mathbf{k} + \mathbf{g} + \mathbf{G}_{1}} e^{-i\mathbf{G}_{1} \cdot \boldsymbol{\tau}_{1\alpha}} e^{-ip_{z}z_{1}} \right.$$

$$\left. + \psi_{n2\alpha\mathbf{g}}^{\xi}(\mathbf{k}) \delta_{\mathbf{p}_{\parallel}, \mathbf{k} + \mathbf{g} + \mathbf{G}_{2}} e^{-i[\mathbf{G}_{1} \cdot (\boldsymbol{\tau}_{1\alpha} - \boldsymbol{\tau}) + \mathbf{G}_{2} \cdot \mathbf{d}]} e^{-ip_{z}z_{2}} \right].$$

$$(8)$$

Here G_1 is a reciprocal lattice vector of the first layer and $G_2 = \mathcal{R}_{-\theta}G_1$ is the corresponding reciprocal lattice vector of the second layer. We take $z_1 = d/2$ and $z_2 = -d/2$, where d = 0.34 nm is the adjacent layer distance. For initial AB-stacking, $\tau = \tau_{1B} = (0, a/\sqrt{3})$.

Taking photon polarization effects into account, the ARPES intensity is the same as in Eq. (4) with the free-electron final state projected to the Bloch state basis:

$$|\mathbf{p}\rangle = \phi^{*}(\mathbf{p}) \sum_{\alpha,\mathbf{g}} \left[\delta_{\mathbf{p}_{\parallel},\mathbf{k}+\mathbf{g}+\mathbf{G}_{1}} e^{i\mathbf{G}_{1}\cdot\boldsymbol{\tau}_{1\alpha}} e^{ip_{z}d/2} |\mathbf{k}+\mathbf{g}, 1\alpha\rangle \right.$$

$$\left. + \delta_{\mathbf{p}_{\parallel},\mathbf{k}+\mathbf{g}+\mathbf{G}_{2}} e^{i[\mathbf{G}_{1}\cdot(\boldsymbol{\tau}_{1\alpha}-\boldsymbol{\tau})+\mathbf{G}_{2}\cdot\mathbf{d}]} e^{-ip_{z}d/2} |\mathbf{k}+\mathbf{g}, 2\alpha\rangle \right].$$

$$(9)$$

Each photoelectron momentum ${\bf p}$ picks a specific valley ξ , a reciprocal lattice vector ${\bf G}_1$ and a moiré reciprocal lattice vector ${\bf g}$ to map ${\bf k}$ into the first MBZ. The ARPES contour becomes complex, depending on ${\bf \tau}$ and ${\bf d}$, for ${\bf G}_2={\cal R}_{-\theta}{\bf G}_1\neq 0$. We therefore focus only on photoelectron momenta ${\bf p}$ near ${\bf K}_+=(4\pi/3a,0)$, the most intense signal comes from ${\bf G}_1={\bf G}_1'={\bf G}_2'=0$. Thus, the ARPES intensity is proportional to

$$I(\mathbf{p}, E) \propto \sum_{n, \mathbf{k}} \left| \sum_{\alpha, \mathbf{g}} \delta_{\mathbf{p}_{\parallel}, \mathbf{k} + \mathbf{g}} (\psi_{n1\alpha\mathbf{g}}^{+}(\mathbf{k}) e^{-ip_{\varepsilon}d/2} + \psi_{n2\alpha\mathbf{g}}^{+}(\mathbf{k}) e^{ip_{\varepsilon}d/2}) \right|^{2} \delta(E - \varepsilon_{n\mathbf{k}}^{+}).$$
(10)

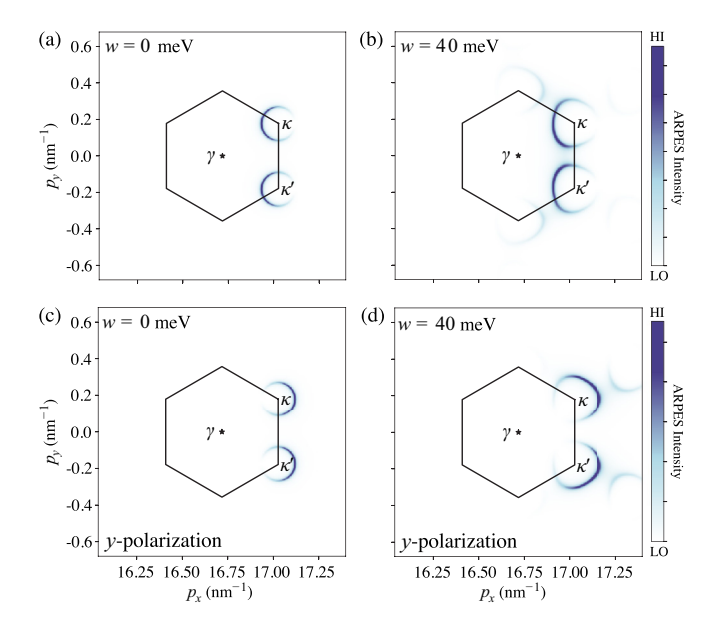


FIG. 3. Constant-energy ARPES momentum distribution of 1.2° -TBG with $v_{\rm F}=10^6$ m/s at energy E=-60 meV (a) without interlayer tunneling and (b) with interlayer tunneling strength w=40 meV. (The experimental tunneling strength is thought to be close to $w\sim110$ meV. Since the continuum model moiré bands depend only on the ratio of w to the twist angle, these results also apply to TBG with a realistic interlayer tunneling amplitude at a twist angle $\sim3^{\circ}$ after rescaling of momentum measured from the Dirac point.) As the interlayer tunneling is turned on, the ARPES signal begins to reflect the altered wave functions and dispersions of the moiré minibands. Band flattening leads to more rapid dependence of the momentum distribution function on energy. (c), (d) corresponds to (a), (b), respectively, using y-polarized light.

Interlayer interference becomes important for large photon energies because $p_z d$ is not negligible, which is the case we are considering to employ the free-electron final state approximation. For a 100 eV photon, the out-of-plane momentum of the photoelectron emitted near the BZ corner is $p_z \sim 5 \text{ Å}^{-1}$. The ARPES intensity $I(\mathbf{p}, E)$ depends periodically on p_z and thereby on photon energy, in analogy to the bilayer graphene case illuminated in Appendix B. We will ignore the photonenergy dependence of ARPES intensity calculations in the remaining part of the paper.

The principle elements of the TBG photoemission signal near valley \mathbf{K}_{+} are illustrated in Fig. 3. When the two graphene layers are artificially decoupled, the individual layer Dirac cones are displaced in momentum space and centered on the displaced BZ corners, $\kappa = \mathcal{R}_{\theta/2} \mathbf{K}_{+}$ and $\kappa' = \mathcal{R}_{-\theta/2} \mathbf{K}_{+}$, of two layers. As shown in Fig. 3(a), two Dirac cones appear at κ , which is the first layer Dirac point, and at κ' , which is the second layer Dirac point. As illustrated in Fig. 3(b), when interlayer tunneling w is turned on the circular constant energy surfaces of the decoupled layers are distorted, and replicas displaced by moiré reciprocal lattice vectors appear that have different matrix elements. The interlayer tunneling strength $w = 40 \,\mathrm{meV}$ chosen in Fig. 3(b) corresponds to the moderate coupling strength present above the first magic twist angle. All TBG calculations in this paper take the Fermi velocity to be $v_{\rm F} = 10^6$ m/s. The appropriate value of w, including its many-body renormalization, plays a key role in TBG electronic properties. These figures show that if the twist angle is known, a numerical value of w can be estimated from ARPES momentum distribution functions.

The anisotropies of the ARPES momentum distribution functions around κ and κ' in Figs. 3(a) and 3(b) can be understood in terms of interference of patterns sourced from two sublattices in each layer:

$$I_l(\mathbf{p}) \propto \cos^2\left(-\frac{\mathbf{p}\cdot(\boldsymbol{\tau}_{l\mathrm{B}}-\boldsymbol{\tau}_{l\mathrm{A}})}{2} + \frac{\xi}{2}\left(\theta_{\mathbf{q}}^l - \theta_l\right) + \frac{\pi(1-s)}{4}\right).$$

The pattern is analogous to the monolayer graphene case illustrated in Appendix A, except that two graphene layers here have a relative twist. $\theta_{\bf q}^l$ is the angle of momentum ${\bf q}$ measured from the Dirac point of layer l, θ_l is the twist angle of layer l ($\theta_1=\theta/2$, $\theta_2=-\theta/2$). In the first layer, for example, $\tau_{1\rm A}=(0,0)$, $\tau_{1\rm B}=\mathcal{R}_{\theta/2}\tau_{\rm B}=e^{i(\pi+\theta)/2}a/\sqrt{3}$, and ${\bf p}={\bf K}_1^++{\bf q}$. Then

$$\mathbf{p} \cdot (\mathbf{\tau}_{1B} - \mathbf{\tau}_{1A}) = (\mathbf{K}_1^+ + \mathbf{q}) \cdot \mathbf{\tau}_{1B} = \mathbf{q} \cdot \mathbf{\tau}_{1B}. \tag{12}$$

Thus, for the valence band in valley +: $\xi = 1$, s = -1, and the minimum of intensity occurs when $\theta_{\mathbf{q}} - \theta/2 - \mathbf{q} \cdot \tau_{1B} = 0$:

$$\theta_{\mathbf{q}} - \frac{\theta}{2} = \frac{qa}{\sqrt{3}} \sin\left(\theta_{\mathbf{q}} - \frac{\theta}{2}\right).$$
 (13)

Equation (13) has the solution $\theta_{\mathbf{q}} = \theta/2$ if $q \ll |\mathbf{G}|$. The anisotropy of photoemission discussed above for the monolayer case is reoriented by the graphene layer twists, providing a handle to measure twist angles from ARPES spectra.

The ARPES momentum distributions with y-polarized light corresponding to Figs. 3(a) and 3(b) are shown in Figs. 3(c) and 3(d). Comparing Figs. 3(a) and 3(c), the photon-polarization dependent anisotropy as a result of the interference between intralayer sublattices bears resemblance to that of monolayer graphene (Appendix A). In addition, comparing Figs. 3(b) and 3(d), we see that the interference between interlayer sublattices rotates in the y-polarization case and shifts the overall minibands anisotropies.

At the first magic twist angle, interlayer tunneling dominates the physics. The ARPES signal at energies in the flat bands is discussed at length in the following section, but there is a strong influence not only on the flat bands but also on the remote bands, whose quasiparticles wave functions have nontrivial momentum space structure manifested by complex momentum distribution functions like those illustrated in Fig. 4. This figure highlights the dependence on an important phenomenological parameter often used in continuum models of TBG, the ratio of the interlayer tunneling amplitude between π -orbitals on the same sublattice w^{AA} to the tunneling amplitude between π -orbitals on different sublattices w^{AB} . These amplitudes are equal by symmetry when strain relaxation of the twisted bilayers is neglected [6], and important strain features can be captured [94–98] by letting $w^{\rm AA}$ be smaller than w^{AB} . The correction accounts partially [99,100] for strain and corrugation effects, neglected in simple bilayer models. The ratio $\alpha = w^{AA}/w^{AB}$ is used as a parameter in the calculations below. Tight-binding model estimates [95] suggest that $\alpha \approx 0.8$, but this estimate should be checked experimentally. α might also be altered by electron-electron

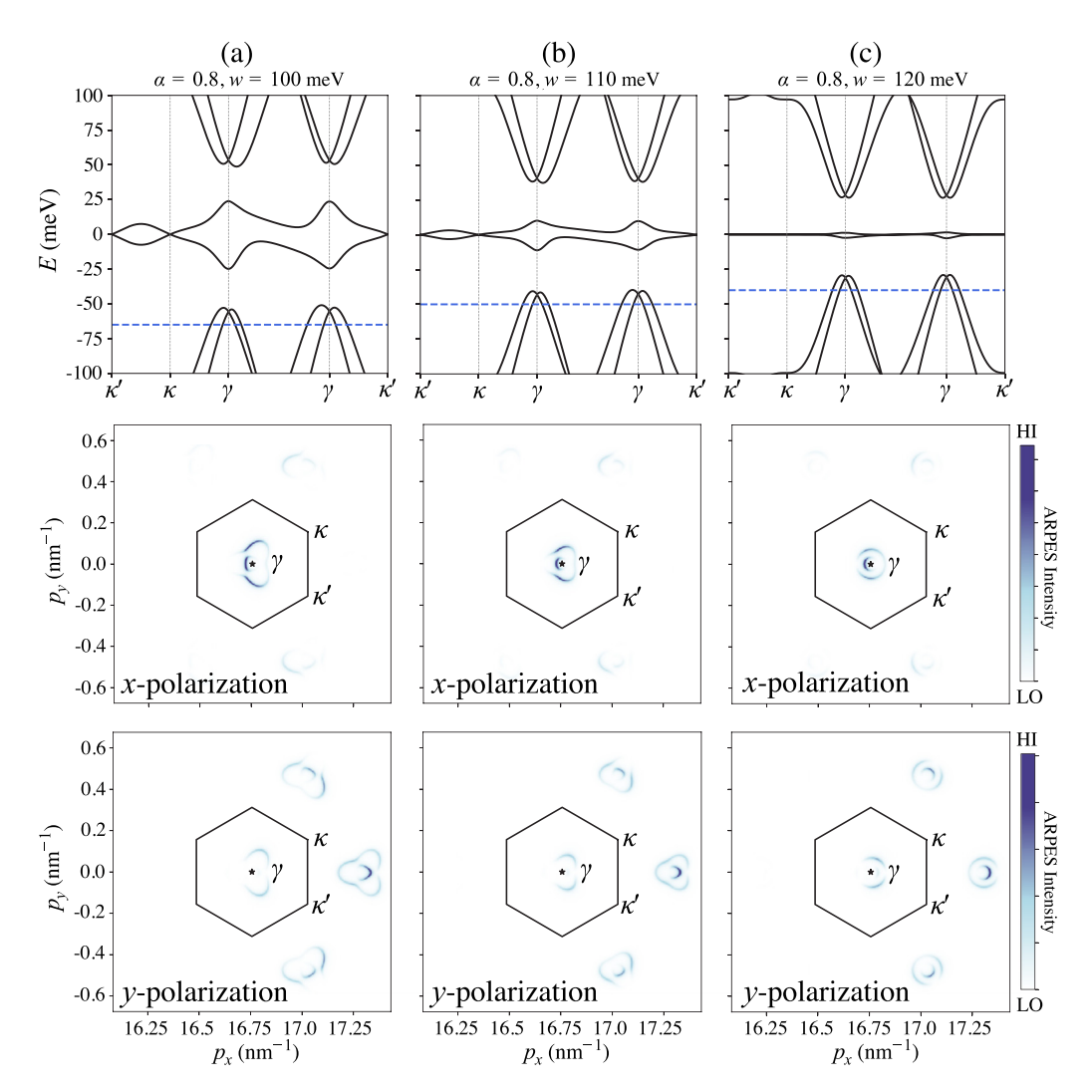


FIG. 4. Band structures and constant-energy ARPES momentum distributions for 1.05° -TBG with tunneling ratio $\alpha = w^{AA}/w^{AB} = 0.8$, and tunneling strength $w = w^{AB}$. The momentum space maps are calculated at the energy near the top of the remote valence bands specified by the blue dashed line in the band structure plots. (a) Tunneling strength w = 100 meV, (b) w = 110 meV, (c) w = 120 meV.

interaction effects. Figures 4 and 5 compare band structures of 1.05° -TBG, and momentum distribution functions calculated at energy levels away from flat interval for different tunneling strengths $w=w^{\rm AB}$ and for tunneling ratios $\alpha=0.8$ (Fig. 4) and $\alpha=1$ (Fig. 5). The energies at which the momentum distributions are calculated are indicated in the band structure plots by blue dashed lines. As in the G/hBN [72,73,78] case, there are secondary Dirac cones at the moiré γ point indicated in Fig. 4 at which isolated layer bands are degenerate. We see in Fig. 5 that the signature of the secondary Dirac cones becomes less prominent as $\alpha \to 1$, providing a handle to choose the best values of this parameter. The proximity of the magic twist angle, which depends on the product of θ and w, can also be detected by examining the remote bands, as illustrated in Figs. 4 and 5.

Theory [14,101–103] and scanning probe experiments [104–107] suggest that broken C_3 rotational symmetry is common when the Fermi level is in the middle of the flat bands of MATBG or when the strain induced by substrate is considered. The constant energy maps in Figs. 4 and 5 retain C_3 rotational symmetry, but because of matrix element effects

the intensity does not. By using the polarized light, described in Appendix A and Eq. (4), the full shape of constant-energy ARPES contours can be seen as shown in Figs 4 and 5.

V. VAN HOVE SINGULARITIES

So far we have discussed momentum distribution functions measured at energies outside the flat bands. The most powerful experimental information will come from measurements within partially occupied flat bands, although these will also require the most precise energy resolution. The dispersion that remains within the flat bands near the magic angle, where they attain their minimum width, is very sensitive to details of the single-particle band structure calculations, including especially filling-factor dependent band renormalizations [104–108] due to mean-field Hartree and exchange interactions [13–15,109]. It is also known that the flat band spectrum is very sensitive to the strain parameter α . Below we calculate for reference ARPES momentum distribution functions at selected energies within the flat bands when the interaction effects are neglected. These calculations are

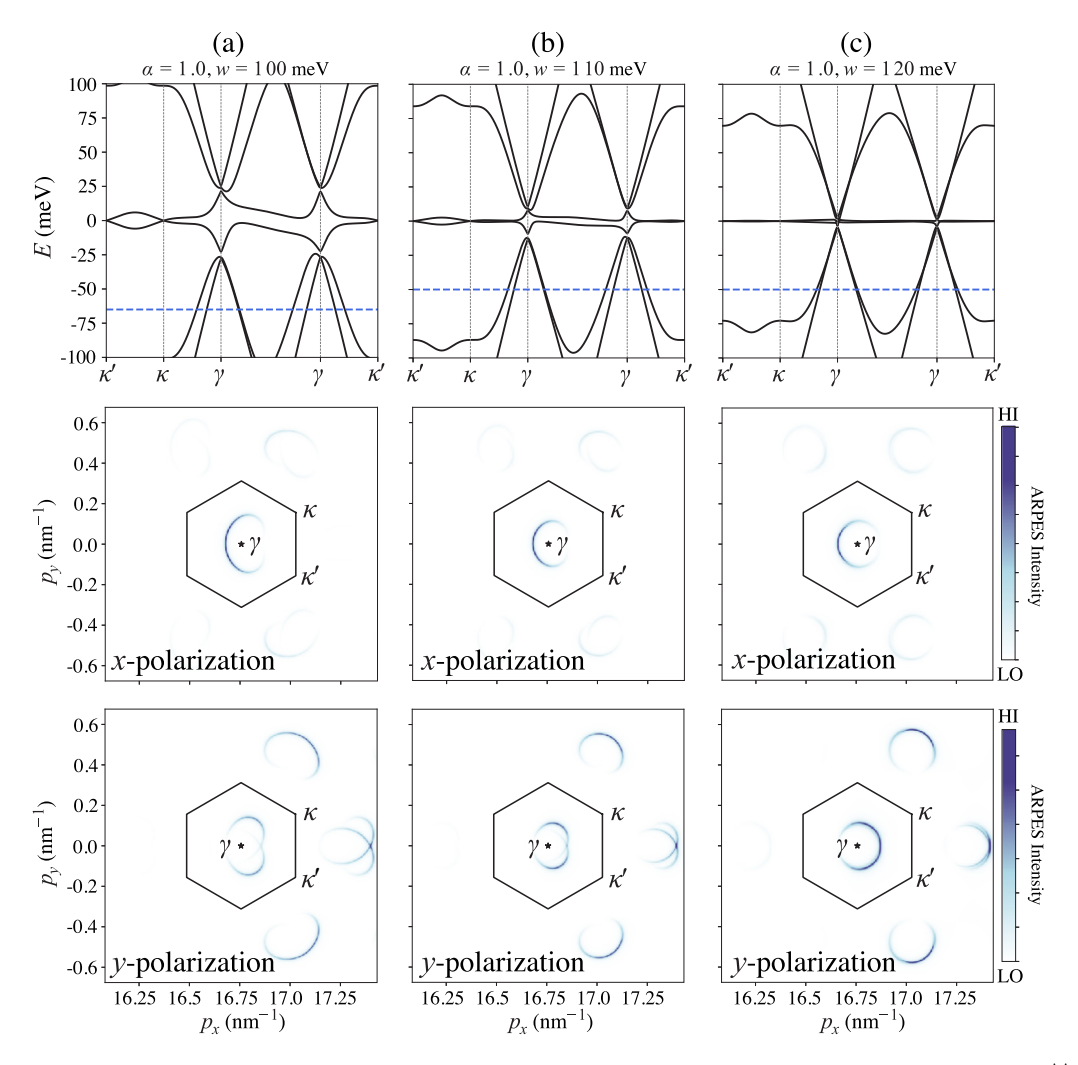


FIG. 5. Band structures and constant-energy ARPES momentum distributions of 1.05° -TBG with tunneling ratio $\alpha = w^{AA}/w^{AB} = 1$, and tunneling strength $w = w^{AB}$. The momentum distribution functions were evaluated at energy levels indicated by the blue dashed lines in the band structures. (a) Tunneling strength w = 100 meV, (b) w = 110 meV, (c) w = 120 meV.

most likely to be relevant when the bilayer is surrounded by nearby conducting layers, for example gate layers, that screen Coulomb interactions strongly.

When interactions are neglected the most prominent feature of the flat bands are the van Hove singularities (VHSs) that occur at Lifshitz phase transition energies [110], which in the past have been studied mainly outside of the flat-band regime. When they are weak compared to the flat band width, the influence of interactions is prominent only for Fermi energies close to VHSs where they can lead to competing broken symmetry states [111–119]. Tuning the Fermi level across a VHS, generally leads to a change in Fermi surface topology. The band filling factors at which VHSs occur in MATBG are strongly sensitive to band structure details that are not always accurately known, and could be identified by performing gatevoltage-dependent ARPES measurements. For example, the continuum model band structures in Fig. 6(a), calculated at $\theta = 2^{\circ}$ and $\alpha = 0, 0.5$, and 1, have valence band van Hove singularities at energies marked by dashed lines. At this twist angle there are three VHSs along the γ - μ lines in the MBZ. Because of the change in constant-energy surface topology from γ -centered electron pockets at energies below the VHS to κ - and κ' -centered hole pockets above the VHS, ARPES momentum distribution functions can distinguish whether a constant energy surface is below or above the VHS energy, as illustrated in Figs. 6(b)–6(d). When $\alpha=0$, i.e., the interlayer tunneling between the same sublattice $w^{AA}=0$, the VHS is exactly at the μ point. As α increases, the VHS position moves away from the μ point along the $\gamma-\mu$ lines as illustrated in Figs. 6(e)–6(g).

At smaller twist angle near the magic angle regime, for example 1.1° , the flat band energy scales are reduced, as shown in Fig. 7(a), but the valence band constant energy surface topology, as shown in Figs. 7(d)–7(f), remains similar as larger twist angles. Near the magic angle, each VHS on the γ - μ line splits into two VHSs [109,120]. In Figs. 7(b), 7(c), and 7(e), we fix twist angle to be 1.1° while tuning the tunneling strength w. Increasing w plays the same role as decreasing twist angle in the low-energy continuum model. In Fig. 7(e), the VHSs start to split.

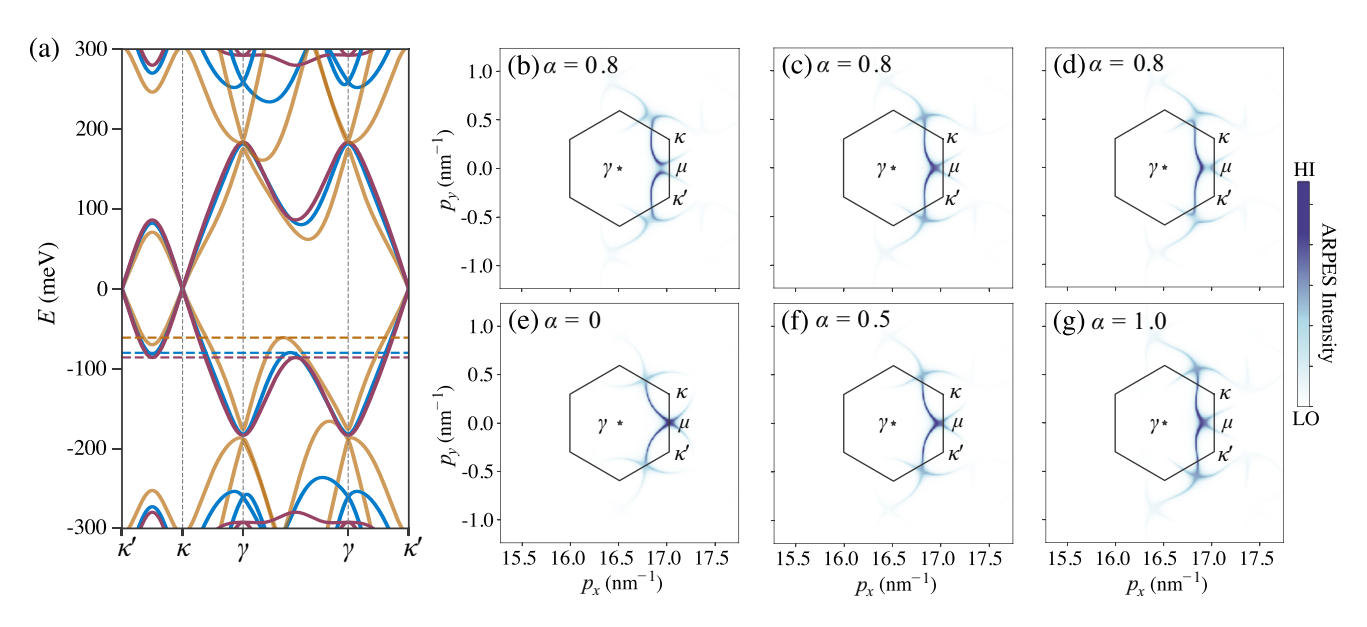


FIG. 6. (a) Band structures of 2° -TBG with tunneling ratio $\alpha=0$ (red), $\alpha=0.5$ (blue) and $\alpha=1$ (yellow). The colored dashed lines mark the corresponding valence band VHS energies. (b)–(d) Constant-energy ARPES maps of 2° -TBG with $\alpha=0.8$ for three energy levels near the valence band VHS. (b) At 2 meV above the valence band VHS, (c) at the valence band VHS energy, (d) at 2 meV below the valence band VHS. (e)–(g) Constant-energy ARPES maps of 2° -TBG at the valence band VHS for different tunneling ratios. (e) $\alpha=0$, (f) $\alpha=0.5$, (g) $\alpha=1.0$. The VHSs are always on the $\gamma-\mu$ high symmetry lines and strong lattice relaxation (small α) moves the VHS towards the μ points of the MBZ. When $\alpha=0$, VHSs are exactly on μ points. All of these calculations were performed with tunneling strength w=110 meV.

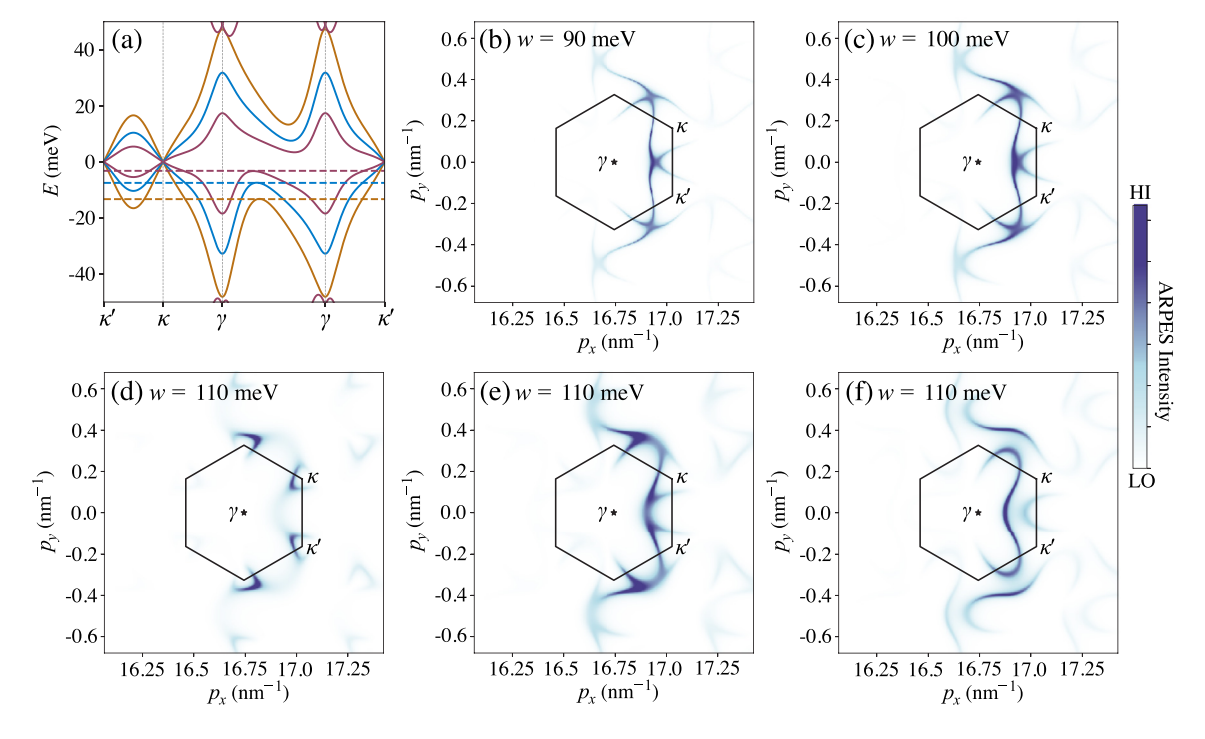


FIG. 7. (a) Band structure of 1.1° -TBG with $\alpha=0.8$ and three different tunneling strengths w=90 meV(yellow), w=100 meV(blue), and w=110 meV(red). The colored dashed lines mark the corresponding valence band VHSs, which are not on the κ - κ' line. (b), (c), (e) Constant-energy maps momentum distribution functions at the valence band VHS energies for 1.1° -TBG with $\alpha=0.8$. (b) w=90 meV, (c) w=100 meV, and (e) w=110 meV. (d)–(f) Constant-energy maps near the valence band VHS of 1.1° -TBG with $\alpha=0.8$ and w=110 meV. The momentum distribution functions (d) at 1 meV above the valence band VHS, (e) at the valence band VHS, (f) and at 1 meV below the valence band VHS illustrates how the constant energy surface topology changes.

VI. DISCUSSION

In this paper we have analyzed how valence band ARPES momentum distribution functions depend on graphene moiré superlattice band Hamiltonians. For G/hBN the critical parameter is the value of the mass parameter m_0 which expresses the degree to which inversion symmetry in the graphene sheet is violated by interaction with the substrate. We point out that m_0 parameter, thought to be key to the quantum anomalous Hall effect, can be extracted from measurements of the anisotropy of the momentum space distribution maps at energies close to the charge neutrality. Since momentumspace anisotropy decreases when m_0 is larger than the conduction-valence band splitting at $m_0 = 0$ (see Fig. 2), finer momentum-space resolution will be needed to identify smaller values of m_0 . The reduced anisotropy is due to weaker interference between honeycomb sublattices with increasing m_0 . For TBG moiré superlattices, the important strain-dependent parameter α that characterizes the ratio of intrasublattice to intersublattice tunneling between layers is available from measurements deep in the valence band, which do not require exceptional energy resolution. For this reason we expect that nano-ARPES performed on moiré superlattice samples, which are typically less than 100 μ m in size, can provide important information about moiré superlattice electronic structure, and guide us toward accurate parameter values for low-energy model even before extreme energy resolution is achieved.

That said, the full potential impact of ARPES in understanding MATBG will be realized only if sufficient energy resolution can be achieved in momentum-resolved spectra taken with partially occupied flat bands. Existing results from STM [104–108] suggest that useful results will require an energy resolution scale that is small, perhaps very small, compared to the \sim 40 meV width the flat bands broaden to when partially occupied. Key questions that need to be answered, and can potentially be answered by ARPES, include the following: (i) Is the valence band minimum at γ as it is in single-particle theory, or elsewhere in the MBZ? (ii) Are large Fermi surface reconstructions associated with broken spin and/or valley symmetries at both integer and fractional moiré band fillings as suggested by weak-field Hall transport measurements? (iii) Do the broken spin and/or valley symmetries thought to be necessary for interaction-induced insulating states persist to noninteger band filling factors, including those where superconductivity is observed? (iv) Finally, are there well-defined Fermi surfaces at metallic filling factors with large quasiparticle normalization factors, and if so, what is their shape. The history of progress in advancing ARPES techniques over recent decades suggests that we be optimistic about their application to graphene-based moiré superlattices.

ACKNOWLEDGMENTS

This research was primarily supported by the National Science Foundation through the Center for Dynamics and Control of Materials: an NSF MRSEC under Cooperative Agreement No. DMR-1720595. We acknowledge helpful interactions with Dan Dessau, Eli Rotenberg, and Simon Moser.

APPENDIX A: ARPES IN MONOLAYER GRAPHENE

Accurate calculations of photoemission matrix elements are often challenging. In the free-electron final state approximation, the photoemission process promotes an electron with crystal momentum ${\bf k}$ from the a Bloch state of the target material to a free-space state with momentum ${\bf p}$. The ejected electron is called a photoelectron. In a π -orbital tight-binding model, the initial state of this photoemission process is a Bloch state with π -orbital amplitudes on both sublattices of monolayer graphene's 2D honeycomb lattices. Using a ${\bf k} \cdot {\bf p}$ description of low energy states in the graphene sheet's π -band, the initial Bloch state's are labelled by valley $\xi = \pm$ and band n = c (conduction) or v (valence):

$$|\xi, n, \mathbf{k}\rangle = \sum_{\alpha = \text{A.B}} \psi_{n\alpha}^{\xi}(\mathbf{k}) |\mathbf{k}, \alpha\rangle,$$
 (A1)

where \mathbf{k} is the full momentum measured from the Brillouin zone (BZ) center Γ . The transition amplitude to the final free-particle state is

$$\langle \mathbf{p}|\xi, n, \mathbf{k}\rangle = \frac{1}{\sqrt{N}} \sum_{\mathbf{p}, \sigma} \psi_{n\alpha}^{\xi}(\mathbf{k}) e^{i(\mathbf{k} - \mathbf{p}_{\parallel}) \cdot (\mathbf{R} + \tau_{\alpha})} \phi(\mathbf{p}),$$
 (A2)

where $\phi(\mathbf{p}) = \int d^3\mathbf{r} e^{-i\mathbf{p}\cdot(\mathbf{r}-\mathbf{R}-\tau_\alpha)}\phi(\mathbf{r}-\mathbf{R}-\tau_\alpha)$ is the Fourier transform of atomic π -orbital on sublattice α at lattice vector \mathbf{R} and \mathbf{p}_{\parallel} is the in-plane projection of 3D momentum \mathbf{p} . Dropping factors that depend on the photon polarization and measuring energy relative to a convenient zero, it follows that the ARPES intensity

$$I(\mathbf{p}, E) \propto \sum_{\xi, n, \mathbf{k}} |\langle \mathbf{p} | \xi, n, \mathbf{k} \rangle|^2 \delta(E - \varepsilon_{n\mathbf{k}}^{\xi})$$

$$\propto |\phi(\mathbf{p})|^2 \sum_{\xi, n, \mathbf{k}} \left| \sum_{\alpha} \psi_{n\alpha}^{\xi}(\mathbf{k}) \delta_{\mathbf{p}_{\parallel}, \mathbf{k} + \mathbf{G}} e^{-i\mathbf{G} \cdot \mathbf{\tau}_{\alpha}} \right|^2$$

$$\times \delta(E - \varepsilon_{n\mathbf{k}}^{\xi}), \tag{A3}$$

where G is a reciprocal lattice vector of graphene. For each photoelectron momentum p, the most intense signal comes from the closest extended-zone valley. The photoemission process picks a specific valley and a specific G to map k into the first BZ.

Constant-energy photoemission maps at E=-120 meV and E=-1200 meV are shown in Figs. 8(a) and 8(b) for \mathbf{p}_{\parallel} near $\mathbf{K}_{+}=(4\pi/3a,0)$ (a) and over the full first BZ (b). The anisotropy of ARPES signal in Fig. 8 can be understood as a two-source interference pattern from two sublattices [68],

$$I(\mathbf{p}) \propto \cos^2 \left[-\frac{\mathbf{p}_{\parallel} \cdot (\mathbf{\tau}_{\mathrm{B}} - \mathbf{\tau}_{\mathrm{A}})}{2} + \frac{\xi \theta_{\mathbf{q}}}{2} + \frac{\pi (1 - n)}{4} \right], (A4)$$

n=+1(-1) denotes conduction(valence) band. $\tau_{\rm A}=(0,0),$ $\tau_{\rm B}=(0,a/\sqrt{3}).$ $\theta_{\bf q}$ is the angle of wave vector ${\bf q}$ measured from BZ corners.

The anisotropy is also reflected by directly substituting eigenvectors of the Dirac Hamiltonian in Eq. (A3):

$$\psi_s^{\xi}(\mathbf{q}) = \frac{1}{\sqrt{2}} \left(\frac{e^{-i\xi\theta_{\mathbf{q}}/2}}{ne^{i\xi\theta_{\mathbf{q}}/2}} \right),\tag{A5}$$

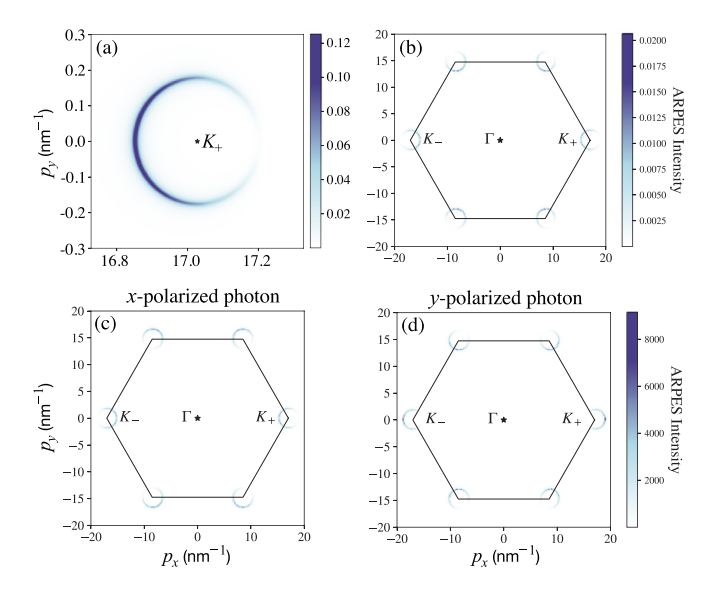


FIG. 8. Constant-energy ARPES maps of monolayer graphene, ignoring photon's polarization effects, at (a) E=-120 meV near \mathbf{K}_+ ; (b) E=-1200 meV for photoelectron momentum \mathbf{p} in the range of the first BZ (hexagon). Constant-energy ARPES maps of monolayer graphene at E=-1200 meV using (c) x-polarized light and (d) y-polarized light.

to obtain

$$I(\mathbf{p}) \propto |e^{-i\xi\theta_{\mathbf{q}}/2}e^{i\mathbf{G}\cdot(\boldsymbol{\tau}_{\mathrm{B}}-\boldsymbol{\tau}_{\mathrm{A}})/2} + ne^{i\xi\theta_{\mathbf{q}}/2}e^{-i\mathbf{G}\cdot(\boldsymbol{\tau}_{\mathrm{B}}-\boldsymbol{\tau}_{\mathrm{A}})/2}|^{2}$$

$$\times \delta_{\mathbf{p}_{\parallel},\mathbf{q}+\mathbf{K}_{\xi}+\mathbf{G}}$$

$$\propto \cos^{2}\left(\frac{-\mathbf{G}\cdot(\boldsymbol{\tau}_{\mathrm{B}}-\boldsymbol{\tau}_{\mathrm{A}})}{2} + \frac{\xi\theta_{\mathbf{q}}}{2} + \frac{\pi(1-n)}{4}\right)$$

$$\times \delta_{\mathbf{p}_{\parallel},\mathbf{q}+\mathbf{K}_{\xi}+\mathbf{G}}.$$
(A6)

When the photon's polarization **A** is explicitly taken into account, the ARPES intensity is proportional to $|\langle \mathbf{p}|\mathbf{A}\cdot\hat{\mathbf{v}}|\xi,n,\mathbf{k}\rangle|^2$, where $\hat{\mathbf{v}}=\nabla_{\mathbf{k}}H$ [69] is the velocity operator and $|\mathbf{p}\rangle$ is the free-electron final state projected to the Bloch state basis

$$|\mathbf{p}\rangle = \sum_{\mathbf{k},\alpha} |\mathbf{k},\alpha\rangle\langle\mathbf{k},\alpha|\mathbf{p}\rangle$$

$$= \sum_{\mathbf{k},\alpha} \delta_{\mathbf{p}_{\parallel},\mathbf{k}+\mathbf{G}} e^{i\mathbf{G}\cdot\mathbf{\tau}_{\alpha}} \phi^{*}(\mathbf{p})|\mathbf{k},\alpha\rangle. \tag{A7}$$

Specifically, the constant-energy ARPES intensity is

$$I(\mathbf{p}, E) \propto \sum_{\xi, n, \mathbf{k}} |\langle \mathbf{p} | \mathbf{A} \cdot \hat{\mathbf{v}} | \xi, n, \mathbf{k} \rangle|^2 \delta(E - \varepsilon_{n\mathbf{k}}^{\xi})$$

$$= \sum_{\xi, n, \mathbf{k}} |\mathbf{A} \cdot \langle \mathbf{p} | \nabla_{\mathbf{k}} H | \xi, n, \mathbf{k} \rangle|^2 \delta(E - \varepsilon_{n\mathbf{k}}^{\xi}). \quad (A8)$$

Figures 8(c) and 8(d) plot the constant-energy ARPES signals using x- and y-polarized light, respectively. The anisotropies can be understood by substituting $\nabla_{\mathbf{k}} H \propto$

 $(\xi \sigma_x, \sigma_y)$ in Eq. (A8), which gives

$$I^{x\text{-pol}}(\mathbf{p}) \propto \cos^{2}\left(\frac{\mathbf{G} \cdot (\boldsymbol{\tau}_{B} - \boldsymbol{\tau}_{A})}{2} + \frac{\xi \theta_{\mathbf{q}}}{2} + \frac{\pi(1-n)}{4}\right)$$

$$\times \delta_{\mathbf{p}_{\parallel},\mathbf{q} + \mathbf{K}_{\xi} + \mathbf{G}},$$

$$I^{y\text{-pol}}(\mathbf{p}) \propto \cos^{2}\left(\frac{\mathbf{G} \cdot (\boldsymbol{\tau}_{B} - \boldsymbol{\tau}_{A})}{2} + \frac{\xi \theta_{\mathbf{q}}}{2} + \frac{\pi(1+n)}{4}\right)$$

$$\times \delta_{\mathbf{p}_{\parallel},\mathbf{q} + \mathbf{K}_{\xi} + \mathbf{G}}.$$
(A9)

APPENDIX B: ARPES IN BILAYER GRAPHENE

We comment here on the importance of reaching a consensus on the signs of hopping amplitudes in graphene multi-layers. For Bernal-stacked bilayer graphene, multiple studies adopted interlayer hoppings with wrong signs [68,121–130] in the π -orbital tight-binding model. As Ref. [131] clarified, not only the magnitudes but also the signs of hopping parameters play a crucial role in electronic properties. We will show that the signs of intralayer and interlayer hoppings can be identified by careful ARPES measurements.

Using the four-component spinor basis, $\Psi_{\mathbf{k}} = (c_{1A}, c_{1B}, c_{2A}, c_{2B})^T$, with layer (1,2) and sublattice (A, B) degrees of freedom, the Hamiltonian of Bernal-stacked bilayer graphene is

$$H(\mathbf{k}) = \begin{pmatrix} \varepsilon_{1A} & t_0 f(\mathbf{k}) & t_4 f(\mathbf{k}) & t_3 f^*(\mathbf{k}) \\ t_0 f^*(\mathbf{k}) & \varepsilon_{1B} & t_1 & t_4 f(\mathbf{k}) \\ t_4 f^*(\mathbf{k}) & t_1 & \varepsilon_{2A} & t_0 f(\mathbf{k}) \\ t_3 f(\mathbf{k}) & t_4 f^*(\mathbf{k}) & t_0 f^*(\mathbf{k}) & \varepsilon_{2B} \end{pmatrix}, \quad (B1)$$

where

$$f(\mathbf{k}) = \sum_{j=1}^{3} e^{i\mathbf{k}\cdot\delta_j},$$
 (B2)

 δ_j is the position of B sublattice relative to A sublattice. t_0 is the intralayer nearest-neighbor (NN) hopping parameter, t_1 is the interlayer hopping between dimer sites and t_3 and t_4 are interlayer next-nearest-neighbor (NNN) hopping parameters between nondimer sites:

$$t_{0} = \langle \mathbf{R}_{1A} | \mathcal{H} | \mathbf{R}_{1B} \rangle = \langle \mathbf{R}_{2A} | \mathcal{H} | \mathbf{R}_{2B} \rangle,$$

$$t_{1} = \langle \mathbf{R}_{1B} | \mathcal{H} | \mathbf{R}_{2A} \rangle,$$

$$t_{3} = \langle \mathbf{R}_{1A} | \mathcal{H} | \mathbf{R}_{2B} \rangle,$$

$$t_{4} = \langle \mathbf{R}_{1A} | \mathcal{H} | \mathbf{R}_{2A} \rangle = \langle \mathbf{R}_{1B} | \mathcal{H} | \mathbf{R}_{2B} \rangle.$$
(B3)

 $|\mathbf{R}_{\alpha}\rangle$ is localized Wannier orbitals. t_0 is related to the Fermi velocity by $v_{\rm F} = \sqrt{3}a|t_0|/2\hbar$, t_1 and t_3 determine the amplitude and orientation of trigonal warping and t_4 introduces particle-hole asymmetry.

Reference [131] ascertained that, using the maximally localized Wannier wave-function method, t_0 is negative and t_1 , t_3 and t_4 are positive. The negative sign of t_0 and positive sign of t_1 have been testified by polarization-dependent ARPES measurements in Ref. [31].

The signs of t_3 and t_4 can also be determined by photon-polarization-dependent ARPES using Eq. (A8). Figure 9 show constant-energy ARPES contours near valley

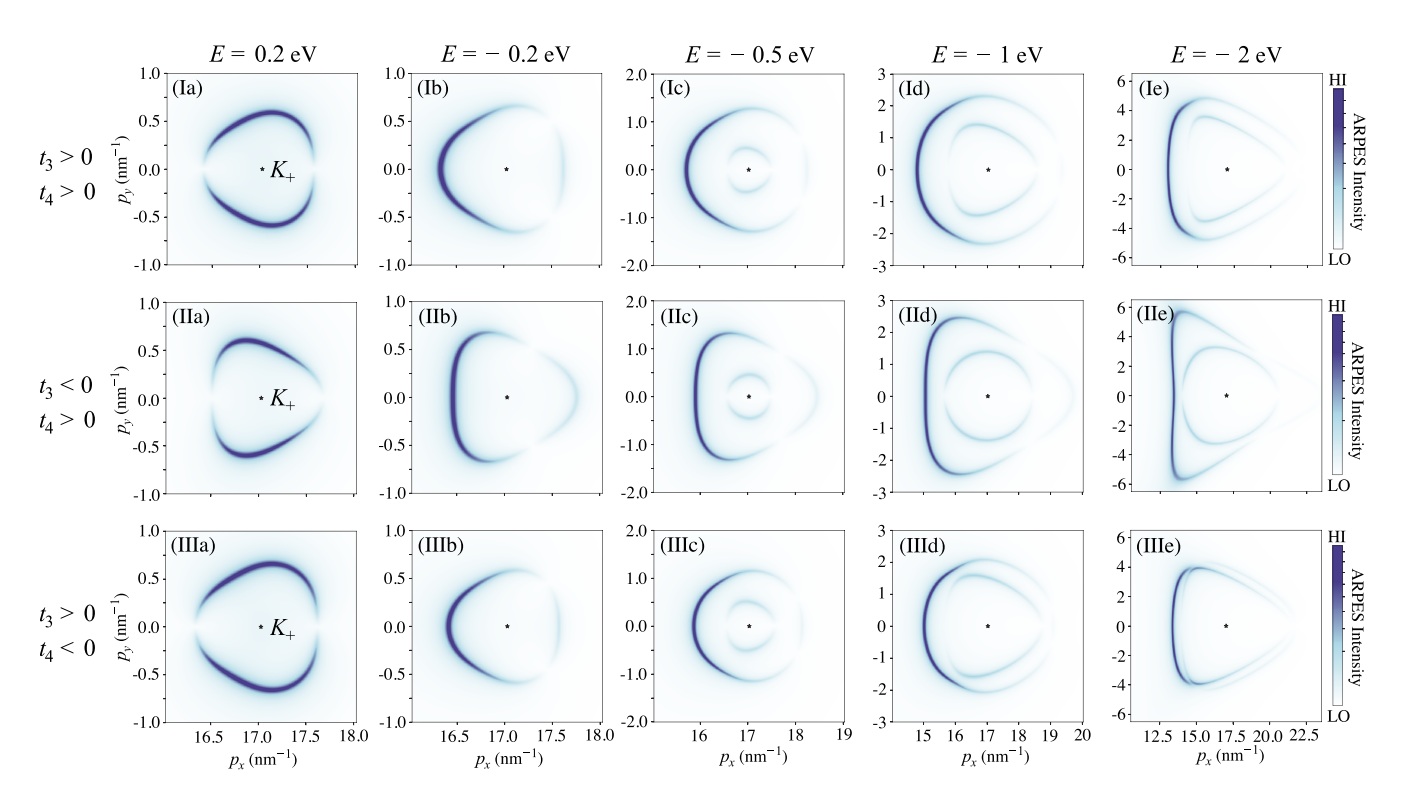


FIG. 9. Constant-energy ARPES momentum distributions, using *x*-polarized light, near \mathbf{K}_+ at various energies indicated at the top of each column. We use *ab initio* tight-binding parameters in Ref. [131], $t_0 = -2.61$ eV, $t_1 = 0.361$ eV, $t_3 = 0.283$ eV, and $t_4 = 0.138$ eV. (Ia)–(Ie) $t_3 > 0$, $t_4 > 0$; (IIa)–(IIe) $t_3 < 0$, $t_4 > 0$; (IIIa)–(IIIe) $t_3 < 0$, $t_4 < 0$. Note that we use a power-law normalized color bar.

 $\mathbf{K}_{+} = (4\pi/3a, 0)$, using x-polarized [31] beam, for different signs of t_3 and t_4 at various energies. For positive t_3 [Figs. 9(Ia)–9(Ie) and 9(IIIa)–9(IIIe)], the trigonal warping orientations of the highest valence band and lowest conduction band are inverted as the Fermi level is tuned away from the charge neutrality, while the trigonal warping orientations of the lowest valence band and highest conduction band stay the same. For negative t_3 [Figs. 9(IIa)–9(IIe)], the trigonal warping orientations of the highest valence band and lowest conduction band stay invariant as tuning the Fermi level, and the trigonal warpings of the lowest valence band and highest conduction band are less evident. The opposite sign of t_4 interchanges conduction and valence bands, as shown in the band structure in Fig. 10. Two conduction bands intersect for positive t_4 and two valence bands intersect for negative t₄. Figure 11 show constant-energy ARPES contours with y-polarized light. By comparing Figs. 9 and 11 with ARPES experiments [23,31], it is inferred that $t_0 < 0$, $t_1 > 0$, $t_3 > 0$, and $t_4 > 0$. This result can also be found in recent scanning tunneling microscopy experiment [132].

With the correct hopping signs discussed above, Fig. 12 shows constant-energy ARPES momentum distributions near the first BZ [Figs. 12(Ia)-12(Ic)] and zoom-in figures near valley K_+ [Figs. 12(IIa)-12(IIc)]. Figures in columns a,b and c are calculated ignoring photon polarization, and with x-polarized light and with y-polarized light, respectively. In multilayer systems, including the bilayer graphene we are discussing here and the TBG in Secs. IV and V in the main text, interference between orbitals in different layers results in photon-energy-dependent ARPES signal. Interlayer interference becomes important when the photon energy is large

enough that $p_z d \sim 1$, where d is the adjacent layer distance and p_z is the z-component of photoelectron momentum. With this consideration, the ARPES intensity becomes

$$I(\mathbf{p}, E) \propto |\phi(\mathbf{p})|^2 \sum_{n, \mathbf{k}} \left| \sum_{\alpha} \psi_{n\alpha}(\mathbf{k}) \delta_{\mathbf{p}_{\parallel}, \mathbf{k}} e^{-ip_z \hat{z} \cdot \mathbf{\tau}_{\alpha}} \right|^2 \delta(E - \varepsilon_{n\mathbf{k}}),$$
(B4)

 $\psi_{n\alpha}(\mathbf{k})$ is the eigenvector of Hamiltonian Eq. (B1), and α represents layer and sublattice indices. In accordance with

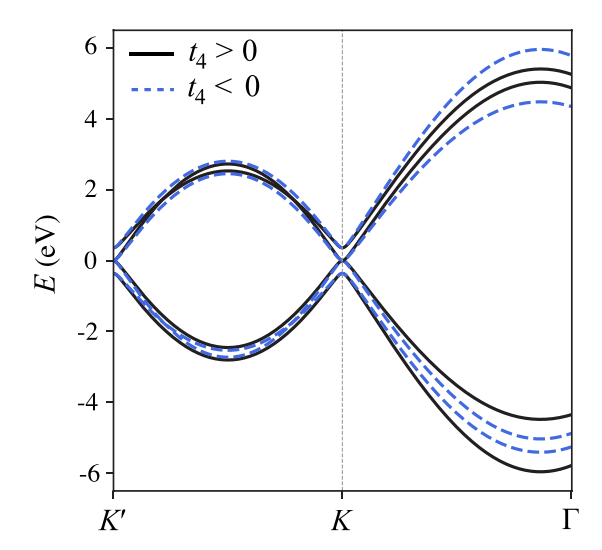


FIG. 10. Band structure of Bernal-stacked bilayer graphene with positive t_4 (solid black line) and negative t_4 (blue dashed line).

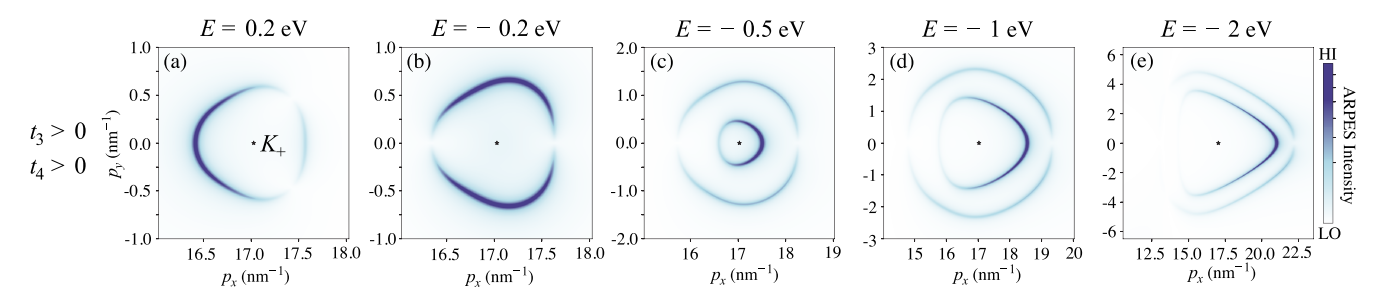


FIG. 11. Constant-energy ARPES momentum distributions, using y-polarized light, near \mathbf{K}_+ at various energies. The tight-binding parameters are the same as in Figs. 9(Ia)-9(Ie). Note that we use a power-law normalized color bar.

Hamiltonian Eq. (B1),

$$\tau_{1A} = \left(0, 0, \frac{d}{2}\right), \quad \tau_{1B} = \left(0, \frac{a}{\sqrt{3}}, \frac{d}{2}\right),
\tau_{2A} = \left(0, \frac{a}{\sqrt{3}}, -\frac{d}{2}\right), \quad \tau_{2B} = \left(0, \frac{2a}{\sqrt{3}}, -\frac{d}{2}\right). \quad (B5)$$

 p_z is related to photoelectron's kinetic energy $E_{\rm kin}$ by

$$\frac{\hbar^2}{2m}(p_{\parallel}^2 + p_z^2) = E_{\rm kin} = \hbar\omega + E - \phi,$$
 (B6)

where $\hbar\omega$ is photon energy, E is the initial Bloch state energy measured relative to the Fermi energy and ϕ is the work function. For large enough photon's energy $\hbar\omega$,

$$p_z \approx \sqrt{\frac{2m\hbar\omega}{\hbar^2} - p_{\parallel}^2}.$$
 (B7)

Fixed $p_y = 0$, Figs. 12(IIIa)–12(IIIc) show ARPES intensities near the BZ corner \mathbf{K}_+ as a function of p_z and p_x . Photon's energy ranges from 20 to 210 eV in Figs. 12(IIIa)–12(IIIc).

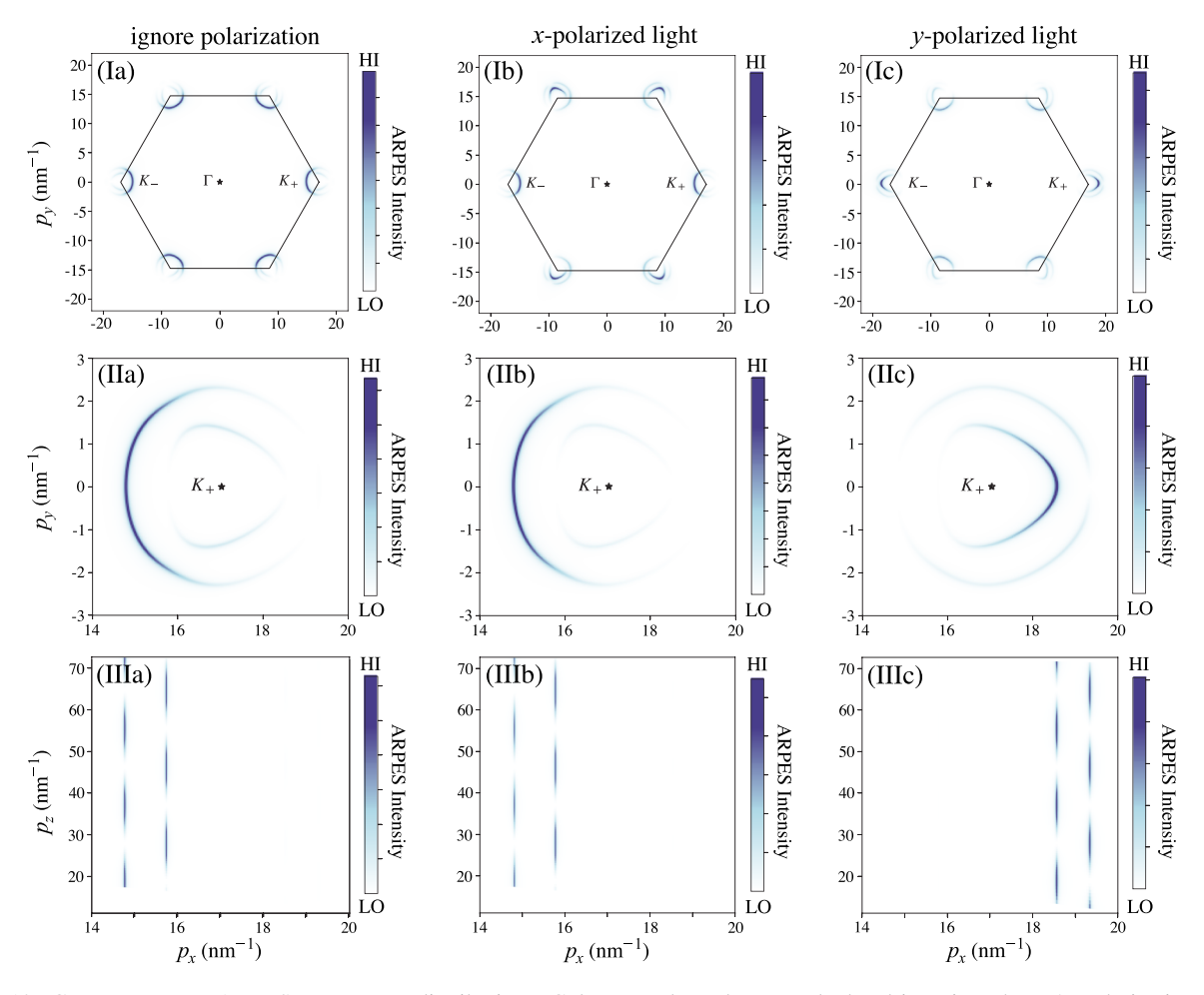


FIG. 12. Constant-energy ARPES momentum distributions. Columns a, b, and c are calculated ignoring photon's polarization, with x-polarized light and with y-polarized light, respectively. (Ia), (Ib), (Ic) are near the first BZ. (IIa), (IIb), (IIc) are near the BZ corner \mathbf{K}_+ . (IIIa), (IIIb), (IIIc) are near \mathbf{K}_+ and calculated with fixed $p_y = 0$, photon's energy $\hbar\omega$ ranges from 20 to 210 eV. p_z is related to $\hbar\omega$ by Eq. (B7). All figures are calculated with $t_0 = -2.61$ eV, $t_1 = 0.361$ eV, $t_3 = 0.283$ eV, and $t_4 = 0.138$ eV. Note that the scales of color bars are different.

- [1] K. S. Novoselov, A. K. Geim, S. V. Morozov, D. Jiang, Y. Zhang, S. V. Dubonos, I. V. Grigorieva, and A. A. Firsov, Science 306, 666 (2004).
- [2] A. K. Geim and K. S. Novoselov, Nat. Mater. 6, 183 (2007).
- [3] C. R. Dean, A. F. Young, I. Meric, C. Lee, L. Wang, S. Sorgenfrei, K. Watanabe, T. Taniguchi, P. Kim, K. L. Shepard, and J. Hone, Nat. Nanotechnol. 5, 722 (2010).
- [4] C. R. Dean, A. Young, L. Wang, I. Meric, G.-H. Lee, K. Watanabe, T. Taniguchi, K. Shepard, P. Kim, and J. Hone, Solid State Commun. 152, 1275 (2012).
- [5] J. Xue, J. Sanchez-Yamagishi, D. Bulmash, P. Jacquod, A. Deshpande, K. Watanabe, T. Taniguchi, P. Jarillo-Herrero, and B. J. LeRoy, Nat. Mater. 10, 282 (2011).
- [6] R. Bistritzer and A. H. MacDonald, Proc. Natl. Acad. Sci. USA 108, 12233 (2011).
- [7] Y. Cao, V. Fatemi, S. Fang, K. Watanabe, T. Taniguchi, E. Kaxiras, and P. Jarillo-Herrero, Nature (London) 556, 43 (2018).
- [8] Y. Cao, V. Fatemi, A. Demir, S. ang, S. L. Tomarken, J. Y. Luo, J. D. Sanchez-Yamagishi, K. Watanabe, T. Taniguchi, E. Kaxiras, R. C. Ashoori, and P. Jarillo-Herrero, Nature (London) 556, 80 (2018).
- [9] X. Lu, P. Stepanov, W. Yang, M. Xie, M. A. Aamir, I. Das, C. Urgell, K. Watanabe, T. Taniguchi, G. Zhang, A. Bachtold, A. H. MacDonald, and D. K. Efetov, Nature (London) 574, 653 (2019).
- [10] M. Yankowitz, S. Chen, H. Polshyn, Y. Zhang, K. Watanabe, T. Taniguchi, D. Graf, A. F. Young, and C. R. Dean, Science 363, 1059 (2019).
- [11] A. L. Sharpe, E. J. Fox, A. W. Barnard, J. Finney, K. Watanabe, T. Taniguchi, M. A. Kastner, and D. Goldhaber-Gordon, Science 365, 605 (2019).
- [12] M. Serlin, C. L. Tschirhart, H. Polshyn, Y. Zhang, J. Zhu, K. Watanabe, T. Taniguchi, L. Balents, and A. F. Young, Science 367, 900 (2020).
- [13] F. Guinea and N. R. Walet, Proc. Natl. Acad. Sci. USA 115, 13174 (2018).
- [14] M. Xie and A. H. MacDonald, Phys. Rev. Lett. 124, 097601 (2020).
- [15] M. Xie and A. H. MacDonald, arXiv:2010.07928.
- [16] H. C. Po, L. Zou, A. Vishwanath, and T. Senthil, Phys. Rev. X 8, 031089 (2018).
- [17] N. Bultinck, E. Khalaf, S. Liu, S. Chatterjee, A. Vishwanath, and M. P. Zaletel, Phys. Rev. X 10, 031034 (2020).
- [18] Y.-Z. You and A. Vishwanath, npj Quantum Mater. 4, 16 (2019).
- [19] A. Damascelli, Z. Hussain, and Z.-X. Shen, Rev. Mod. Phys. 75, 473 (2003).
- [20] I. M. Vishik, W. S. Lee, R.-H. He, M. Hashimoto, Z. Hussain, T. P. Devereaux, and Z.-X. Shen, New J. Phys. 12, 105008 (2010).
- [21] D. Lu, I. M. Vishik, M. Yi, Y. Chen, R. G. Moore, and Z.-X. Shen, Annu. Rev. Condens. Matter Phys. 3, 129 (2012).
- [22] Y. Xia, D. Qian, D. Hsieh, L. Wray, A. Pal, H. Lin, A. Bansil, D. Grauer, Y. S. Hor, R. J. Cava, and M. Z. Hasan, Nat. Phys. 5, 398 (2009).
- [23] T. Ohta, A. Bostwick, T. Seyller, K. Horn, and E. Rotenberg, Science 313, 951 (2006).
- [24] T. Ohta, A. Bostwick, J. L. McChesney, T. Seyller, K. Horn, and E. Rotenberg, Phys. Rev. Lett. 98, 206802 (2007).

- [25] M. Sprinkle, D. Siegel, Y. Hu, J. Hicks, A. Tejeda, A. Taleb-Ibrahimi, P. Le Fèvre, F. Bertran, S. Vizzini, H. Enriquez, S. Chiang, P. Soukiassian, C. Berger, W. A. de Heer, A. Lanzara, and E. H. Conrad, Phys. Rev. Lett. 103, 226803 (2009).
- [26] A. Bostwick, T. Ohta, T. Seyller, K. Horn, and E. Rotenberg, Nat. Phys. 3, 36 (2007).
- [27] A. Bostwick, T. Ohta, J. L. McChesney, K. V. Emtsev, T. Seyller, K. Horn, and E. Rotenberg, New J. Phys. 9, 385 (2007).
- [28] S. Y. Zhou, G.-H. Gweon, A. V. Fedorov, P. N. First, W. A. de Heer, D.-H. Lee, F. Guinea, A. H. Castro Neto, and A. Lanzara, Nat. Mater. 6, 770 (2007).
- [29] A. Bostwick, T. Ohta, T. Seyller, K. Horn, and E. Rotenberg, arXiv:cond-mat/0609660v1.
- [30] C. Coletti, S. Forti, A. Principi, K. V. Emtsev, A. A. Zakharov, K. M. Daniels, B. K. Daas, M. V. S. Chandrashekhar, T. Ouisse, D. Chaussende, A. H. MacDonald, M. Polini, and U. Starke, Phys. Rev. B 88, 155439 (2013).
- [31] C. Hwang, C.-H. Park, D. A. Siegel, A. V. Fedorov, S. G. Louie, and A. Lanzara, Phys. Rev. B 84, 125422 (2011).
- [32] I. Gierz, J. Henk, H. Höchst, C. R. Ast, and K. Kern, Phys. Rev. B 83, 121408(R) (2011).
- [33] T. Ohta, J. T. Robinson, P. J. Feibelman, A. Bostwick, E. Rotenberg, and T. E. Beechem, Phys. Rev. Lett. 109, 186807 (2012).
- [34] K. S. Kim, A. L. Walter, L. Moreschini, T. Seyller, K. Horn, E. Rotenberg, and A. Bostwick, Nat. Mater. 12, 887 (2013).
- [35] S.-K. Mo, Nano Converg. 4, 6 (2017).
- [36] P. Dudin, P. Lacovig, C. Fava, E. Nicolini, A. Bianco, G. Cautero, and A. Barinov, J. Synchrotron Radiat. 17, 445 (2010).
- [37] A. Bostwick, E. Rotenberg, J. Avila, and M. C. Asensio, Synchrotron Radiat. News 25, 19 (2012).
- [38] J. Avila, I. Razado-Colambo, S. Lorcy, J.-L. Giorgetta, F. Polack, and M. C. Asensio, J. Phys.: Conf. Ser. 425, 132013 (2013).
- [39] J. Avila, I. Razado-Colambo, S. Lorcy, B. Lagarde, J.-L. Giorgetta, F. Polack, and M. C. Asensio, J. Phys.: Conf. Ser. 425, 192023 (2013).
- [40] J. Avila, I. Razado, S. Lorcy, R. Fleurier, E. Pichonat, D. Vignaud, X. Wallart, and M. C. Asensio, Sci. Rep. 3, 2439 (2013).
- [41] J. Avila and M. C. Asensio, Synchrotron Radiat. News 27, 24 (2014).
- [42] H. Coy Diaz, J. Avila, C. Chen, R. Addou, M. C. Asensio, and M. Batzill, Nano Lett. 15, 1135 (2015).
- [43] F. Joucken, Eberth A. Quezada-López, J. Avila, C. Chen, J. L. Davenport, H. Chen, K. Watanabe, T. Taniguchi, M. C. Asensio, and J. Velasco, Phys. Rev. B 99, 161406(R) (2019).
- [44] C. Chen, J. Avila, S. Wang, Y. Wang, M. Mucha-Kruczyński, C. Shen, R. Yang, B. Nosarzewski, T. P. Devereaux, G. Zhang, and M. C. Asensio, Nano Lett. 18, 1082 (2018).
- [45] J. Katoch, S. Ulstrup, R. J. Koch, S. Moser, K. M. McCreary, S. Singh, J. Xu, B. T. Jonker, R. K. Kawakami, A. Bostwick, E. Rotenberg, and C. Jozwiak, Nat. Phys. 14, 355 (2018).
- [46] F. Joucken, J. Avila, Z. Ge, E. A. Quezada-Lopez, H. Yi, R. Le Goff, E. Baudin, J. L. Davenport, K. Watanabe, T. Taniguchi, M. C. Asensio, and J. Velasco, Nano Lett. 19, 2682 (2019).
- [47] P. V. Nguyen, N. C. Teutsch, N. P. Wilson, J. Kahn, X. Xia, A. J. Graham, V. Kandyba, A. Giampietri, A. Barinov,

- G. C. Constantinescu, N. Yeung, N. D. M. Hine, X. Xu, D. H. Cobden, and N. R. Wilson, Nature (London) 572, 220 (2019).
- [48] E. Wang, G. Chen, G. Wan, X. Lu, C. Chen, J. Avila, A. V. Fedorov, G. Zhang, M. C. Asensio, Y. Zhang, and S. Zhou, J. Phys.: Condens. Matter 28, 444002 (2016).
- [49] S. Lisi, X. Lu, T. Benschop, T. A. de Jong, P. Stepanov, J. R. Duran, F. Margot, I. Cucchi, E. Cappelli, A. Hunter, A. Tamai, V. Kandyba, A. Giampietri, A. Barinov, J. Jobst, V. Stalman, M. Leeuwenhoek, K. Watanabe, T. Taniguchi, L. Rademaker et al., arXiv:2002.02289.
- [50] M. I. B. Utama, R. J. Koch, K. Lee, N. Leconte, H. Li, S. Zhao, L. Jiang, J. Zhu, K. Watanabe, T. Taniguchi, P. D. Ashby, A. Weber-Bargioni, A. Zettl, C. Jozwiak, J. Jung, E. Rotenberg, A. Bostwick, and F. Wang, Nat. Phys. 17, 184 (2021).
- [51] I. Razado-Colambo, J. Avila, J.-P. Nys, C. Chen, X. Wallart, M.-C. Asensio, and D. Vignaud, Sci. Rep. 6, 27261 (2016).
- [52] B. Amorim, Phys. Rev. B 97, 165414 (2018).
- [53] B. Amorim and E. V. Castro, arXiv:1807.11909.
- [54] A. Pal and E. J. Mele, Phys. Rev. B 87, 205444 (2013).
- [55] M. Mucha-Kruczyński, J. R. Wallbank, and V. I. Fal'ko, Phys. Rev. B 93, 085409 (2016).
- [56] J. Jung, A. Raoux, Z. Qiao, and A. H. MacDonald, Phys. Rev. B 89, 205414 (2014).
- [57] J. Jung, E. Laksono, A. M. DaSilva, A. H. MacDonald, M. Mucha-Kruczyński, and S. Adam, Phys. Rev. B 96, 085442 (2017).
- [58] J. Jung, A. M. DaSilva, A. H. MacDonald, and S. Adam, Nat. Commun. 6, 6308 (2015).
- [59] V. N. Strocov, M. Shi, M. Kobayashi, C. Monney, X. Wang, J. Krempasky, T. Schmitt, L. Patthey, H. Berger, and P. Blaha, Phys. Rev. Lett. 109, 086401 (2012).
- [60] A. Damascelli, Phys. Scr. **T109**, 61 (2004).
- [61] P. Puschnig, S. Berkebile, A. J. Fleming, G. Koller, K. Emtsev, T. Seyller, J. D. Riley, C. Ambrosch-Draxl, F. P. Netzer, and M. G. Ramsey, Science 326, 702 (2009).
- [62] K. Medjanik, O. Fedchenko, S. Chernov, D. Kutnyakhov, M. Ellguth, A. Oelsner, B. Schönhense, T. R. F. Peixoto, P. Lutz, C. H. Min, F. Reinert, S. Däster, Y. Acremann, J. Viefhaus, W. Wurth, H. J. Elmers, and G. Schönhense, Nat. Mater. 16, 615 (2017).
- [63] P. Puschnig and D. Lüftner, J. Electron Spectrosc. Relat. Phenom. 200, 193 (2015), special Anniversary Issue: Volume 200.
- [64] E. L. Shirley, L. J. Terminello, A. Santoni, and F. J. Himpsel, Phys. Rev. B 51, 13614 (1995).
- [65] P. Ayria, A. R. T. Nugraha, E. H. Hasdeo, T. R. Czank, S.-i. Tanaka, and R. Saito, Phys. Rev. B 92, 195148 (2015).
- [66] N. Barrett, E. E. Krasovskii, J.-M. Themlin, and V. N. Strocov, Phys. Rev. B 71, 035427 (2005).
- [67] V. N. Strocov, E. E. Krasovskii, W. Schattke, N. Barrett, H. Berger, D. Schrupp, and R. Claessen, Phys. Rev. B 74, 195125 (2006).
- [68] M. Mucha-Kruczyński, O. Tsyplyatyev, A. Grishin, E. McCann, V. I. Fal'ko, A. Bostwick, and E. Rotenberg, Phys. Rev. B 77, 195403 (2008).
- [69] S. Ismail-Beigi, E. K. Chang, and S. G. Louie, Phys. Rev. Lett. 87, 087402 (2001).
- [70] B. Hunt, J. D. Sanchez-Yamagishi, A. F. Young, M. Yankowitz, B. J. LeRoy, K. Watanabe, T. Taniguchi, P. Moon,

- M. Koshino, P. Jarillo-Herrero, and R. C. Ashoori, Science **340**, 1427 (2013).
- [71] C. R. Woods, L. Britnell, A. Eckmann, R. S. Ma, J. C. Lu, H. M. Guo, X. Lin, G. L. Yu, Y. Cao, R. Gorbachev, A. V. Kretinin, J. Park, L. A. Ponomarenko, M. I. Katsnelson, Y. Gornostyrev, K. Watanabe, T. Taniguchi, C. Casiraghi, H.-J. Gao, A. K. Geim *et al.*, Nat. Phys. 10, 451 (2014).
- [72] L. A. Ponomarenko, R. V. Gorbachev, G. L. Yu, D. C. Elias, R. Jalil, A. A. Patel, A. Mishchenko, A. S. Mayorov, C. R. Woods, J. R. Wallbank, M. Mucha-Kruczynski, B. A. Piot, M. Potemski, I. V. Grigorieva, K. S. Novoselov, F. Guinea, V. I. Fal'ko, and A. K. Geim, Nature (London) 497, 594 (2013).
- [73] C.-H. Park, L. Yang, Y.-W. Son, M. L. Cohen, and S. G. Louie, Phys. Rev. Lett. 101, 126804 (2008).
- [74] A. M. DaSilva, J. Jung, S. Adam, and A. H. MacDonald, Phys. Rev. B 91, 245422 (2015).
- [75] C. Ortix, L. Yang, and J. van den Brink, Phys. Rev. B 86, 081405(R) (2012).
- [76] J. R. Wallbank, A. A. Patel, M. Mucha-Kruczyński, A. K. Geim, and V. I. Fal'ko, Phys. Rev. B 87, 245408 (2013).
- [77] E. Wang, X. Lu, S. Ding, W. Yao, M. Yan, G. Wan, K. Deng, S. Wang, G. Chen, L. Ma, J. Jung, A. V. Fedorov, Y. Zhang, G. Zhang, and S. Zhou, Nat. Phys. 12, 1111 (2016).
- [78] M. Yankowitz, J. Xue, D. Cormode, J. D. Sanchez-Yamagishi, K. Watanabe, T. Taniguchi, P. Jarillo-Herrero, P. Jacquod, and B. J. LeRoy, Nat. Phys. 8, 382 (2012).
- [79] S. Ulstrup, J. C. Johannsen, A. Crepaldi, F. Cilento, M. Zacchigna, C. Cacho, R. T. Chapman, E. Springate, F. Fromm, C. Raidel, T. Seyller, F. Parmigiani, M. Grioni, and P. Hofmann, J. Phys.: Condens. Matter 27, 164206 (2015).
- [80] Y. Liu, G. Bian, T. Miller, and T.-C. Chiang, Phys. Rev. Lett. 107, 166803 (2011).
- [81] S. Moser, J. Electron Spectrosc. Relat. Phenom. 214, 29 (2017).
- [82] I. Gierz, M. Lindroos, H. Höchst, C. R. Ast, and K. Kern, Nano Lett. **12**, 3900 (2012).
- [83] H. Polshyn, J. Zhu, M. A. Kumar, Y. Zhang, F. Yang, C. L. Tschirhart, M. Serlin, K. Watanabe, T. Taniguchi, A. H. MacDonald, and A. F. Young, Nature (London) 588, 66 (2020).
- [84] P. Stepanov, I. Das, X. Lu, A. Fahimniya, K. Watanabe, T. Taniguchi, F. H. L. Koppens, J. Lischner, L. Levitov, and D. K. Efetov, Nature (London) 583, 375 (2020).
- [85] N. Bultinck, S. Chatterjee, and M. P. Zaletel, Phys. Rev. Lett. 124, 166601 (2020).
- [86] Y.-H. Zhang, D. Mao, Y. Cao, P. Jarillo-Herrero, and T. Senthil, Phys. Rev. B **99**, 075127 (2019).
- [87] Y.-H. Zhang, D. Mao, and T. Senthil, Phys. Rev. Research 1, 033126 (2019).
- [88] J. C. W. Song, P. Samutpraphoot, and L. S. Levitov, Proc. Natl. Acad. Sci. USA 112, 10879 (2015).
- [89] D. Xiao, W. Yao, and Q. Niu, Phys. Rev. Lett. 99, 236809 (2007).
- [90] T. M. R. Wolf, O. Zilberberg, I. Levkivskyi, and G. Blatter, Phys. Rev. B 98, 125408 (2018).
- [91] J. Liu and X. Dai, Phys. Rev. B 103, 035427 (2021).
- [92] C. Repellin, Z. Dong, Y.-H. Zhang, and T. Senthil, Phys. Rev. Lett. 124, 187601 (2020).
- [93] F. Wu and S. Das Sarma, Phys. Rev. Lett. 124, 046403 (2020).

- [94] K. Uchida, S. Furuya, J.-I. Iwata, and A. Oshiyama, Phys. Rev. B 90, 155451 (2014).
- [95] M. Koshino, N. F. Q. Yuan, T. Koretsune, M. Ochi, K. Kuroki, and L. Fu, Phys. Rev. X 8, 031087 (2018).
- [96] M. M. van Wijk, A. Schuring, M. I. Katsnelson, and A. Fasolino, 2D Mater. 2, 034010 (2015).
- [97] S. Dai, Y. Xiang, and D. J. Srolovitz, Nano Lett. 16, 5923 (2016).
- [98] S. K. Jain, V. Juričić, and G. T. Barkema, 2D Mater. 4, 015018 (2016).
- [99] S. Carr, S. Fang, Z. Zhu, and E. Kaxiras, Phys. Rev. Research 1, 013001 (2019).
- [100] N. N. T. Nam and M. Koshino, Phys. Rev. B 96, 075311 (2017).
- [101] Z. Bi, N. F. Q. Yuan, and L. Fu, Phys. Rev. B 100, 035448 (2019).
- [102] S. Liu, E. Khalaf, J. Y. Lee, and A. Vishwanath, Phys. Rev. Research 3, 013033 (2021).
- [103] M. J. Klug, New J. Phys. 22, 073016 (2020).
- [104] Y. Jiang, X. Lai, K. Watanabe, T. Taniguchi, K. Haule, J. Mao, and E. Y. Andrei, Nature (London) 573, 91 (2019).
- [105] A. Kerelsky, L. J. McGilly, D. M. Kennes, L. Xian, M. Yankowitz, S. Chen, K. Watanabe, T. Taniguchi, J. Hone, C. Dean, A. Rubio, and A. N. Pasupathy, Nature (London) 572, 95 (2019).
- [106] Y. Choi, J. Kemmer, Y. Peng, A. Thomson, H. Arora, R. Polski, Y. Zhang, H. Ren, J. Alicea, G. Refael, F. von Oppen, K. Watanabe, T. Taniguchi, and S. Nadj-Perge, Nat. Phys. 15, 1174 (2019).
- [107] Y. Xie, B. Lian, B. Jäck, X. Liu, C.-L. Chiu, K. Watanabe, T. Taniguchi, B. A. Bernevig, and A. Yazdani, Nature (London) 572, 101 (2019).
- [108] D. Wong, K. P. Nuckolls, M. Oh, B. Lian, Y. Xie, S. Jeon, K. Watanabe, T. Taniguchi, B. A. Bernevig, and A. Yazdani, Nature (London) 582, 198 (2020).
- [109] T. Cea, N. R. Walet, and F. Guinea, Phys. Rev. B 100, 205113 (2019).
- [110] S. Wu, Z. Zhang, K. Watanabe, T. Taniguchi, and E. Y. Andrei, Nat. Mater. 20, 488 (2021).
- [111] W. Kohn and J. M. Luttinger, Phys. Rev. Lett. 15, 524 (1965).

- [112] R. Markiewicz, J. Phys. Chem. Solids 58, 1179 (1997).
- [113] J. González, Phys. Rev. B 78, 205431 (2008).
- [114] M. Fleck, A. M. Oleś, and L. Hedin, Phys. Rev. B **56**, 3159 (1997)
- [115] T. M. Rice and G. K. Scott, Phys. Rev. Lett. 35, 120 (1975).
- [116] B. Valenzuela and M. A. H. Vozmediano, New J. Phys. 10, 113009 (2008).
- [117] D. Makogon, R. van Gelderen, R. Roldán, and C. M. Smith, Phys. Rev. B 84, 125404 (2011).
- [118] R. Nandkishore, L. S. Levitov, and A. V. Chubukov, Nat. Phys. 8, 158 (2012).
- [119] T. Li, Europhys. Lett. 97, 37001 (2012).
- [120] N. F. Q. Yuan, H. Isobe, and L. Fu, Nat. Commun. 10, 5769 (2019).
- [121] E. McCann and M. Koshino, Rep. Prog. Phys. 76, 056503 (2013).
- [122] I. V. Iorsh, K. Dini, O. V. Kibis, and I. A. Shelykh, Phys. Rev. B 96, 155432 (2017).
- [123] C.-S. Park, Solid State Commun. 152, 2018 (2012).
- [124] A. Grüneis, C. Attaccalite, L. Wirtz, H. Shiozawa, R. Saito, T. Pichler, and A. Rubio, Phys. Rev. B 78, 205425 (2008).
- [125] W. Jolie, J. Lux, M. Pörtner, D. Dombrowski, C. Herbig, T. Knispel, S. Simon, T. Michely, A. Rosch, and C. Busse, Phys. Rev. Lett. 120, 106801 (2018).
- [126] E. McCann and V. I. Fal'ko, Phys. Rev. Lett. 96, 086805 (2006).
- [127] J. Cserti, A. Csordás, and G. Dávid, Phys. Rev. Lett. 99, 066802 (2007).
- [128] J. Jung, F. Zhang, and A. H. MacDonald, Phys. Rev. B 83, 115408 (2011).
- [129] J. Nilsson, A. H. Castro Neto, F. Guinea, and N. M. R. Peres, Phys. Rev. B 78, 045405 (2008).
- [130] E. V. Castro, K. S. Novoselov, S. V. Morozov, N. M. R. Peres, J. M. B. L. dos Santos, J. Nilsson, F. Guinea, A. K. Geim, and A. H. C. Neto, J. Phys.: Condens. Matter 22, 175503 (2010).
- [131] J. Jung and A. H. MacDonald, Phys. Rev. B 89, 035405 (2014).
- [132] F. Joucken, Z. Ge, E. A. Quezada-López, J. L. Davenport, K. Watanabe, T. Taniguchi, and J. Velasco, Phys. Rev. B 101, 161103(R) (2020).